Investigation of three-dimensional effects on a cavitating Venturi flow

Jean Decaix, Eric Goncalvès da Silva

Investigation of three-dimensional effects on a cavitating Venturi flow

Jean Decaix*, Eric Goncalvès

LEGI-Grenoble INP, 1025 rue de la Piscine, 38400 St Martin d'Heres, France

Abstract

A numerical investigation of the behaviour of a cavitation pocket developing along a Venturi geometry has been performed using a compressible one-fluid hybrid RANS/LES solver. The interplay between turbulence and cavitation regarding the unsteadiness and structure of the flow is complex and not well understood. This constitutes a determinant point to accurately simulate the dynamic of sheet cavities. Various turbulent approaches are tested: a new Scale-Adaptive model and the Detached Eddy Simulation. 2D and 3D simulations are compared with the experimental data. An oblique mode of the sheet is put in evidence.

Keywords: Cavitation, Homogeneous model, Scale-Adaptive model, 3D effects, Instabilities

*Corresponding author.
Email address: Jean.Decaix@legi.grenoble-inp.fr (Jean Decaix)

Nomenclature

Abbreviation

CFD Computational Fluid Dynamic

CFL Courant-Friedrichs-Lewy number

DES Detached Eddy Simulation

DFT Direct Fourier Transform

EOS Equation Of State

LES Large Eddy Simulation

PANS Partial Average Navier-Stokes

RANS Reynolds-Average Navier-Stokes

RMS Root Mean Square

SA Spalart and Allmaras turbulence model

SAS Scale-Adaptive Simulation

TBLE Turbulent Boundary Layer Equations

Greek symbols

α Void fraction

ϵ Turbulent dissipation rate

κ Von Karman constant

λ Mixture thermal conductivity

λ_t Mixture turbulent thermal conductivity

μ Mixture dynamic viscosity

μ_t Mixture dynamic eddy viscosity

ρ Mixture density

ρ_L^{sat} Density of liquid at saturation

ρ_V^{sat} Density of vapour at saturation

σ cavitation parameter

$\overline{\overline{\tau}}$ Mixture total stress tensor

$\tilde{\nu}$ Pseudo eddy-viscosity

Latin symbols

C_p Heat capacity at constant pressure

c_{baro} Minimum speed of sound in the mixture

C_{DES} Constant of the DES model

$\tilde{d}$ New distance of the DES model

d Distance to the nearest wall

e Mixture internal energy

F_c Convective flux density

F_v Viscous flux density

k Mixture turbulent kinetic energy

ℓ Integral turbulence length scale

L_{vk} Von Karman length scale

P Mixture pressure

P_k Turbulent production term

Pr Prandtl number

Pr_t Turbulent Prandtl number

Q Mixture total heat flux

Re Reynolds number

S Source term

S_{ij} Stress tensor

T Temperature

u^+ Non dimensional wall velocity

u_i Mass velocity vector

U_τ Friction velocity

w Vector of conservative variables

y^+ Non dimensional wall distance

Subscript

$inlet$ Inlet value

k k-phase

ref Reference value

w Wall value

Superscript

t Turbulent part

v Viscous part

1. Introduction

Cavitation is a significant engineering phenomenon that occurs in fluid machinery, fuel injectors, marine propellers, nozzles, underwater bodies, etc. In most cases, cavitation is an undesirable phenomenon, significantly degrading performance, resulting in reduced flow rates, lower pressure increases in pumps, load asymmetry, vibrations, noise and erosion. Such flows are characterized by important variations of the local Mach number (due to the drastic diminution of the speed of sound in the mixture), large density ratio between the liquid and the vapour phases, small-scale turbulence interactions and non equilibrium thermodynamic states.

A considerable effort has been realized to understand the fundamental physics of cavitation phenomena concerning the dynamics of both sheet and cloud cavitation. Cavitation sheets that appear on solid bodies are characterized by a closure region which always fluctuates, with the presence of a re-entrant jet. This jet is mainly composed of liquid which penetrates the attached cavity from downstream and flows upstream along the solid surface. Partial cavity can be classified as either closed or open attached cavity, depending on the flow in the cavity closure region. A closed partial cavity has a relatively stable cavity length and a cavity closure that is relatively free of bubbles. An open cavity is typically frothy in appearance, and has a periodically varying length that is associated with the shedding of vapour clouds [1]. Both types of cavities have been studied, experimentally and numerically, to describe and investigate the transition between stable and unstable behaviour, the development of the re-entrant jet, the interaction with the turbulent boundary layer, and the mechanism of cloud cavitation generation [2, 3, 4, 5].

Observations on hydrofoils with high-speed motion pictures put in evidence the three-

dimensional structures associated with the phenomena. The re-entrant jet does not progress uniformly toward the leading edge according to the spanwise location, and the jet component normal to the closure line is reflected inward [6]. Studies of the spanwise effect through the sweep angle concluded the re-entrant jet was directed into the cavity allowing for a steady sheet which only sheds cavitating clouds at the far downstream edge [7]. To distinguish between various directions of the re-entrant flow, the term side-entrant jet was introduced. This term refers to the part of the jet that has a strong spanwise velocity component directed into the cavity originating from the sides. The term re-entrant jet is reserved for the flow originating from the part of the cavity where the closure is more or less perpendicular to the incoming flow and is thus mainly directed upstream. The shape of the closure region of the cavity sheet governs the direction of the re-entrant and side-entrant jets. Both jets may form an equally important source for the shedding [8]. The spanwise variation in the cavity and its evolution leads to important variations in the thickness and the void fraction of the sheet. The cloud cavitation structures generated are also fully 3D. The 3D shedding mechanism studied on a twisted hydrofoil marked differences with the 2D shedding, and included secondary instabilities caused by side-entry [8]. Recently, an experimental analysis of a pulsating cavitation sheet made appear the presence of a bifurcation of the cavitation sheet behaviours [9]. To put in evidence this bifurcation, the authors applied the Proper Orthogonal Decomposition (POD) and the Dynamic Mode Decomposition (DMD), which allowed to give the energetic spectrum of the structures and the associated frequency. It seemed that when the cloud shedding mechanism was driven by a shock wave, a low frequency associated with spanwise structures is observed.

Besides these experimental investigations, numerical simulations were performed

to investigate such 3D unsteady cavitating flows on hydrofoils and venturis, based on mixture homogeneous models (one-fluid methods). Various assumptions were done on the viscous effects and the turbulence modelling. Inviscid compressible codes have been developed to simulate the 3D twisted hydrofoil, with a special emphasis on the detection of shock formation and propagation [10], or a study of the dynamics of the phenomena [11]. To investigate the cavitation-turbulence interaction occurring at small scales and the mechanism that generates the large-scale vortex structure, 3D turbulent codes have been developed. Different approaches for the turbulence modelling have been investigated in order to capture the finer-scale dynamics. First computations were performed solving the unsteady Reynolds-Averaged Navier-Stokes (URANS) equations coupled with transport-equation turbulence models. Recently, URANS computations of the 3D twisted hydrofoil showed the ability of such a computation to capture the large scales of the cavitation sheet [12]. As the URANS approach did not fully account for the turbulent-cavitation interactions, Large Eddy Simulations (LES) were tested on both hydrofoil and Venturi geometries [13, 14]. Yet, due to high Reynolds number flows and the significant cost in the computational requirements, simulations were performed on coarse grids which leading to under-resolved simulations. To overcome the high computational cost of a wall resolved LES, a wall model based on the logarithmic law of the wall was introduced in an implicit LES solver [15, 16]. Validations on 3D cavitating cases clearly exhibited secondary cavitating vortices in spite of the small spanwise extension. Another strategy proposed by Spalart, referred to as Detached-Eddy Simulation (DES), enables to simulate smaller scales with a minimal computational cost [17]. First cavitating simulations were proposed for a massively separated hydrofoil [18], but results were far from statistically stationary. Other simulations were performed on ventilated bodies and an ogive [19] where DES appeared to yield more accurate flow mod-

elling. A comparison with URANS, DES and ILES approach was proposed on the twisted cavitating foil [20]. The major mechanisms governing the shedding dynamics were well captured by simulations except for the URANS approach. Recently, the Partial-Averaged Navier-Stokes (PANS) approach based on a $k-\varepsilon$ turbulence model, initially developed for aerodynamic flows, was tested for a cavitating flow around a marine propeller [21] and the twisted hydrofoil [22]. This approach aims at resolving a substantial part of the turbulent fluctuations but does not contain an explicit dependency on the computational grid as LES. It involves the ratio of the unresolved-to-total kinetic energy f_k and the ratio of the unresolved-to-total dissipation rate f_ε in the model constants. The user decides a priori how much of the kinetic energy and dissipation rate is to be modelled.

In previous work, an in-house finite-volume code solving the URANS compressible equations was developed with a mixture homogeneous approach. The cavitation phenomenon was modelled by a barotropic liquid-vapour mixture equation of state (EOS). Preliminary 2D computations were performed to assess the numerical aspects, thermodynamic constraints on the EOS and the influence of various transport-equation turbulence models [23, 24]. Recently, an hybrid RANS/LES model able to adjust the level of turbulent eddy viscosity was developed and validated on 2D Venturi flows [25]. Such a strategy called Scale-Adaptive Simulation (SAS) was introduced by Menter and Egorov (see [26] for a review of the SAS model). From their work, we derived two SAS turbulence models based on one- and two-equation models. As the PANS approach, Scale-Adaptive models do not imply explicitly a dependence on the grid. To compare these models with other hybrid RANS/LES models, computations are performed with the DES approach of Spalart. We performed 2D and 3D computations, which show the advantage of hybrid RANS/LES

turbulence models compared with standard turbulence models. Analyses have been conducted with a special emphasis on the 3D effects. Our goals in this study are:

- To test a new formulation of a scale-adaptive model for cavitating flows and to investigate the behaviour of the proposed model on unsteady cavitating flows.
- To study 3D effects on a Venturi geometry by comparing 2D and 3D simulations.
- To compare SAS and DES for the simulation of cavitating flows.

This paper is organized as follows. We present first the governing equations, including the physical models, followed by an overview of the numerical methods adopted. The Venturi configuration and the associated numerical parameters are then presented. 2D and 3D simulations are described and compared with experimental data. A deeper analysis of the 3D flow simulated with the Scale-adaptive model is proposed and discussed. The last part deals with conclusions and future investigations.

2. Models, equations and numerics

The numerical simulations are carried out using an in-house CFD code solving the one-fluid compressible hybrid RANS/LES system.

2.1. The homogeneous approach

The homogeneous mixture approach is used to model two-phase flows. The phases are assumed to be sufficiently well mixed and the disperse particle size are sufficiently small thereby eliminating any significant relative motion. The phases are strongly coupled and moving at the same velocity. In addition, the phases are assumed to

be in thermal and mechanical equilibrium: they share the same temperature T and the same pressure P. The evolution of the two-phase flow can be described by the conservation laws that employ the representative flow properties as unknowns just as in a single-phase problem. We introduce α_k the void fraction or the averaged fraction of presence of phase k. The density ρ, the center of mass velocity u and the internal energy e for the mixture are defined by [27]:

$$\rho = \sum_k \alpha_k \rho_k \tag{1}$$

$$\rho u_i = \sum_k \alpha_k \rho_k u_{k,i} \tag{2}$$

$$\rho e = \sum_k \alpha_k \rho_k e_k \tag{3}$$

To close the system, an equation of state (EOS) and a thermal relation are necessary to link the pressure and the temperature to the internal energy and the density.

2.2. The cavitation model

To link the pressure to the thermodynamic variables, the stiffened gas EOS is used for pure phases. In the mixture, a barotropic law proposed by Delannoy [28] is considered.

This law is characterized by its maximum slope $1/c_{baro}^2$. The quantity c_{baro} is an adjustable parameter of the model, which can be interpreted as the minimum speed of sound in the mixture.

When the pressure is between $P_{vap} + \Delta P$ and $P_{vap} - \Delta P$, the following relationship applies:

$$P(\alpha) = P_{vap} + \left(\frac{\rho_L^{sat} - \rho_V^{sat}}{2} \right) c_{baro}^2 \, \mathrm{Arcsin}\,(1 - 2\alpha) \tag{4}$$

where ΔP represents the pressure range of the law and, for a void ratio value of 0.5, the pressure is equal to the saturation pressure P_{vap}. This law introduces a small

non-equilibrium effect on the pressure. Moreover, we assume that thermodynamic effects on the cavitation are negligible.

The hyperbolicity and convexity of the EOS have been demonstrated for the inviscid system [23]. The influence of c_{baro} has been studied in previous work. In the present paper, the value of c_{baro} is set to 0.47 m/s, corresponding to a pressure range of $\Delta P = 175$ Pa.

2.3. Hybrid RANS/LES turbulence modelling

For turbulent computations, the Reynolds-Averaged Navier-Stokes equations are used in an hybrid RANS/LES framework, coupled with two-equation turbulence models. For low Mach number applications, an inviscid preconditioning method is necessary [29, 30], based on the modification of the derivative term by a pre-multiplication with a suitable preconditioning matrix P_c. These equations can be expressed as:

$$P_c^{-1}\frac{\partial w}{\partial t} + \operatorname{div}(F_c - F_v) = S \tag{5}$$

$$w = \begin{pmatrix} \rho \\ \rho V \\ \rho E \\ \rho k \\ \rho \Psi \end{pmatrix} \quad ; \quad F_c = \begin{pmatrix} \rho V \\ \rho V \otimes V + p\overline{\overline{I}} \\ (\rho E + p)V \\ \rho k V \\ \rho \Psi V \end{pmatrix} \quad ; \; F_v = \begin{pmatrix} 0 \\ \overline{\overline{\tau^v}} + \overline{\overline{\tau^t}} \\ (\overline{\overline{\tau^v}} + \overline{\overline{\tau^t}}).V - Q^v - Q^t \\ (\mu + \mu_t/\sigma_k)\operatorname{grad} k \\ (\mu + \mu_t/\sigma_\Psi)\operatorname{grad} \Psi \end{pmatrix}$$

where w denotes the conservative variables, F_c and F_v the convective and viscous flux densities and S the source terms, which concern only the transport equations. k is the mixture turbulent kinetic energy and Ψ is a mixture turbulent variable.

The exact expression of the eddy-viscosity μ_t and the source terms depends on the turbulence model as well as constants σ_k and σ_Ψ.
The total stress tensor $\overline{\overline{\tau}}$ is evaluated using the Stokes hypothesis, Newton's law and the Boussinesq assumption. The total heat flux vector Q is obtained from the Fourier law involving a turbulent thermal conductivity λ_t with the constant Prandtl number hypothesis.

$$\begin{aligned} \overline{\overline{\tau}} &= \overline{\overline{\tau^v}} + \overline{\overline{\tau^t}} = (\mu + \mu_t)\left[(\operatorname{grad} V + (\operatorname{grad} V)^t) - \frac{2}{3}(\operatorname{div} V)\overline{\overline{I}}\right] - \frac{2}{3}\rho k\overline{\overline{I}} \\ Q &= Q^v + Q^t = -(\lambda + \lambda_t)\operatorname{grad} T \quad \text{with} \quad \lambda_t = \frac{\mu_t C_p}{P_{rt}} \end{aligned} \tag{6}$$

In pure liquid, the viscosity μ is determined by an exponential law and, in pure vapour, the viscosity follows the Sutherland law. The mixture viscosity is defined as the arithmetic mean of the liquid and vapour viscosities (fluctuations of viscosity are neglected) [27]:

$$\mu_L(T) = \mu_{0_L} \exp(B/T) \tag{7}$$

$$\mu_V(T) = \mu_{0_V} \sqrt{\frac{T}{293}} \frac{1 + T_S/293}{1 + T_S/T} \tag{8}$$

$$\mu(T, \alpha) = \alpha\mu_V(T) + (1 - \alpha)\mu_L(T) \tag{9}$$

where μ_{0_L}, μ_{0_V}, B and T_S are constants.

The mixture thermal conductivity λ is also defined as the arithmetic mean of the liquid and vapour values:

$$\lambda(\alpha) = \alpha\frac{\mu_V C_{pV}}{P_{r_V}} + (1 - \alpha)\frac{\mu_L C_{p_L}}{P_{r_L}} \tag{10}$$

The turbulent Prandtl number P_{rt} is set to 1.

2.4. The turbulence modelling

Computations of cavitating flows with standard turbulence models are unable to capture the unsteadiness of the cavitation sheet and mainly the liquid re-entrant jet along the wall [24]. To capture the liquid re-entrant jet, various approaches have been tested based on a reduction of the eddy viscosity in the mixture. The correction proposed by Reboud [31] for the $k-\epsilon$ model is often used and consists in modifying the computation of the eddy viscosity:

$$\mu_t \;=\; f(\rho) C_\mu f_\mu \frac{k^2}{\epsilon} \quad \text{with} \quad f(\rho) \;=\; \rho_V + \left(\frac{\rho_V - \rho}{\rho_V - \rho_L}\right)^n (\rho_L - \rho_V) \tag{11}$$

The parameter n is usually set to 10.

The use of the Reboud correction showed its ability to compute various cavitating flows [32, 33, 34]. Nevertheless, this correction is empirical and there is no physical proof for a drastic reduction of the eddy viscosity in two-phase flow regions.

In order to improve the turbulence modelling of cavitating flows, one way consists in applying hybrid RANS/LES models known to reduce the eddy viscosity in region where the mesh allows the resolution of a part of the turbulence spectrum. Such hybrid models became popular during the last decade as the family of Detached Eddy Simulation (DES) models [35, 36] and Scale Adaptive (SAS) models developed by Menter and Egorov [37].

In the present work, the DES model is applied following formulation for the pseudo viscosity $\tilde{\nu}$:

$$\begin{aligned} \frac{\partial \rho\widetilde{\nu}}{\partial t} + \frac{\partial}{\partial x_l}\left[\rho\, u_l\, \widetilde{\nu} - \frac{1}{\sigma}\left(\mu + \rho\widetilde{\nu}\right)\frac{\partial \widetilde{\nu}}{\partial x_l}\right] \;&=\; c_{b1}\left(1 - f_{t2}\right)\widetilde{S}\,\rho\,\widetilde{\nu} + \frac{c_{b2}}{\sigma}\frac{\partial \rho\widetilde{\nu}}{\partial x_l}\frac{\partial \widetilde{\nu}}{\partial x_l} \\ &\quad - \left(c_{\omega 1} f_\omega - \frac{c_{b1}}{\kappa^2} f_{t2}\right)\frac{\widetilde{\nu}^2}{\tilde{d}^2} \end{aligned} \tag{12}$$

with $\tilde{d}$ the new distance to walls defined as:

$$\tilde{d} = \min(d, C_{DES}\Delta) \tag{13}$$

where d is the distance from the nearest wall, $\Delta = \max(\Delta x, \Delta y, \Delta z)$ and $C_{DES} = 0.65$.

SAS models follow another approach compared to the DES models since they do not depend explicitly on the mesh. Indeed, revisiting the $k - k\ell$ model proposed by Rotta [38], Menter shows that in inhomogeneous turbulent flows an additional term including the second derivative of the velocity is present. Modelling this new term and applying a variable change, Menter provides a $k - \Phi$ model with $\Phi = \sqrt{k}\ell$:

$$\begin{aligned} \frac{\partial \rho k}{\partial t} + \frac{\partial \rho u_j k}{\partial x_j} &= \rho P_k - c_\mu^{3/4} \rho \frac{k^{3/2}}{\ell} + \frac{\partial}{\partial x_j}\left(\frac{\mu_t}{\sigma_k}\frac{\partial k}{\partial x_j}\right) \\ \frac{\partial \rho \Phi}{\partial t} + \frac{\partial \rho u_j \Phi}{\partial x_j} &= \frac{\Phi}{k}\rho P_k \left(\xi_1 - \xi_2 \left(\frac{\ell}{L_{v\kappa}}\right)^2\right) - \xi_3 \rho k + \frac{\partial}{\partial x_j}\left(\frac{\mu_t}{\sigma_\phi}\frac{\partial \Phi}{\partial x_j}\right) \end{aligned} \quad (14)$$

with:

$$\frac{\mu_t}{\rho} = \nu_t = c_\mu^{1/4}\Phi \quad ; \quad \rho P_k = \mu_t S^2 \quad ; \quad S = \sqrt{2 S_{ij} S_{ij}} \quad ; \quad S_{ij} = \frac{1}{2}\left(\frac{\partial u_i}{\partial x_j} + \frac{\partial u_j}{\partial x_i}\right)$$

and:

$$L_{v\kappa} = \kappa \left|\frac{U'}{U''}\right| \qquad ; \qquad \left|U'\right| = S \qquad ; \qquad \left|U''\right| = \sqrt{\frac{\partial^2 u_i}{\partial x_k^2}\frac{\partial^2 u_i}{\partial x_j^2}}$$

The new term $\xi_2 \left(\frac{\ell}{L_{v\kappa}}\right)^2$ involves the von Karman length scale $L_{v\kappa}$, which acts as an indicator of the inhomogeneity of the flow. Consequently, in region where the flow is highly inhomogeneous, the production of Φ is reduced leading to a decrease of the eddy viscosity. Adapting this model to the well-known $k - \omega$ SST, Menter [37, 39] and also Davidson [40] showed the ability of this model to adjust the level of the eddy viscosity as a function of the resolved scales. From the work of Menter, we derived a SAS formulation for the Smith $k - \ell$ model [25]. This model writes:

$$\frac{\partial \rho k}{\partial t} + \frac{\partial}{\partial x_l}\left[\rho\, u_l k - \left(\mu + \frac{\mu_t}{\sigma_k}\right)\frac{\partial k}{\partial x_l}\right] = \rho P_k - \frac{\rho\,(2k)^{3/2}}{B_1 \ell} - 2\mu\,\frac{\partial \sqrt{k}}{\partial x_l}\frac{\partial \sqrt{k}}{\partial x_l} \quad (15)$$

$$\begin{aligned}\frac{\partial \rho \ell}{\partial t}+\frac{\partial}{\partial x_l}\left[\rho\, u_l \ell-\left(\mu+\frac{\mu_t}{\sigma_l}\right)\frac{\partial \ell}{\partial x_l}\right] &= -\frac{\ell}{k}P_k\xi_2\left(\frac{\ell}{L_{vk}}\right)^2 \\ &+(2-E_2)\frac{\rho\sqrt{2k}}{B_1}\left[1-\left(\frac{\ell}{\kappa d}\right)^2\right] \\ &-\frac{\mu_t}{\sigma_\ell}\frac{1}{\ell}\frac{\partial \ell}{\partial x_l}\frac{\partial \ell}{\partial x_l}\left(\frac{\ell}{\kappa d}\right)^2+\rho\ell\,\frac{\partial u_l}{\partial x_l} \\ &+2\,\frac{\mu_t}{\sigma_\ell}\frac{1}{k}\frac{\partial \ell}{\partial x_l}\frac{\partial k}{\partial x_l} \end{aligned} \tag{16}$$

with the additional term $-\frac{\ell}{k}P_k\xi_2\left(\frac{\ell}{L_{vk}}\right)^2$ and $\xi_2 = 1,47$ as specified by Menter. The others parameters are set to the values defined by Smith [41]. For our computations, the new term is only activated in two-phase flow regions.

In an earlier paper, Menter [42] transformed the $k-\epsilon$ two equation model in a one transport equation for the eddy viscosity ν_t and made appear the von Karman length scale in the destruction term. Inspiring from this work, a SAS formulation for the Spalart-Allmaras one-equation model (SA) is derived. First, the Spalart-Allmaras model is written in a high Reynolds number form:

$$\begin{aligned}\frac{\partial \rho \widetilde{\nu}}{\partial t}+\frac{\partial}{\partial x_l}\left[\rho\, u_l \widetilde{\nu}-\frac{1}{\sigma}\left(\mu+\rho\widetilde{\nu}\right)\frac{\partial \widetilde{\nu}}{\partial x_l}\right] &= c_{b1}\widetilde{S}\,\rho\,\widetilde{\nu}+\frac{c_{b2}}{\sigma}\frac{\partial \rho\widetilde{\nu}}{\partial x_l}\frac{\partial \widetilde{\nu}}{\partial x_l} \\ &-c_{\omega 1}\overline{\rho}\,\frac{\widetilde{\nu}^2}{d^2}\end{aligned} \tag{17}$$

where the last term on the right side is the destruction term with d the distance to the nearest wall. Replacing d by the von Karman length scale allows the model to behave as a SAS model. Indeed, if we balance the production term and the destruction term, we obtain:

$$\tilde{\nu} \propto L_{vk}^2 \tilde{S} \tag{18}$$

therefore the eddy viscosity is proportional to the von Karman length scale and adjusts to the resolved scales. Compared with the DES formulation, this formulation

does not depend explicitly on the mesh. Incorporating this modification in the SA model, the transport-equation for $\tilde{\nu}$ becomes:

$$\begin{aligned}\frac{\partial \rho\widetilde{\nu}}{\partial t}+\frac{\partial}{\partial x_l}\left[\rho\, u_l\,\widetilde{\nu}-\frac{1}{\sigma}\left(\mu+\rho\widetilde{\nu}\right)\frac{\partial\widetilde{\nu}}{\partial x_l}\right] &= c_{b1}\left(1-f_{t2}\right)\widetilde{S}\,\rho\,\widetilde{\nu}+\frac{c_{b2}}{\sigma}\frac{\partial\overline{\rho}\widetilde{\nu}}{\partial x_l}\frac{\partial\widetilde{\nu}}{\partial x_l}\\ &\quad -c_{\omega 1}f_{\omega}\overline{\rho}\,\xi_{sas}\frac{\widetilde{\nu}^2}{L_{vk}^2}\\ &\quad -\frac{c_{b1}}{\kappa^2}f_{t2}\rho\,\frac{\widetilde{\nu}^2}{d^2}\end{aligned} \tag{19}$$

with ξ_{SAS} a constant to specify. In the present work, the use of L_{vk} instead of d is applied only in two-phase flow regions and after several tests, the constant ξ_{SAS} is set to 3.

2.5. Wall functions

At the wall, a two-layer wall law is used:

$$\begin{aligned} u^+ &= y^+ && \text{if} \quad y^+ < 11.13\\ u^+ &= \frac{1}{\kappa}\ln y^+ + 5.25 && \text{if} \quad y^+ > 11.13\\ u^+ &= \frac{u}{U_\tau} \quad ; \quad y^+ = \frac{yU_\tau}{\nu_w} \quad ; \quad U_\tau = \sqrt{\frac{\tau_w}{\rho_w}} \end{aligned} \tag{20}$$

where $\kappa = 0.41$ is the von Karman constant and the subscript w indicates wall values. The wall shear stress τ_w is obtained from the analytical velocity profile (Eq. 20) by iterating on the product y^+u^+. We assume that wall functions are similar in a two-phase flow and in a single-phase flow. The validity of this assumption was studied in [43] for Venturi cavitating flows. Comparisons with the thin boundary layer equations (TBLE) were performed and showed the good behaviour of the two-layer approach. For three-dimensional boundary layers, the existence of a wall law is assumed valid for the streamwise velocity component. Moreover, in adjacent cells

to a wall, the velocity is supposed collinear to the wall friction direction.

With regard to the turbulent transport-equation models, the production of k is computed according to the formulation proposed by Viegas and Rubesin [44]. The value of ℓ in the first cell is computed with the linear relation $\ell = \kappa y$.
For the one-equation Spalart-Allmaras model, the transported quantity is calculated using the model's closure relations, the velocity profile and a mixing-length formulation for the eddy-viscosity (see [43] for more details).

2.6. Numerical methods

The numerical simulations are carried out using an implicit CFD code solving the RANS/turbulent systems for multi-domain structured meshes. This solver is based on a cell-centered finite-volume discretization. For the mean flow, the convective flux density vector on a cell face is computed with the Jameson-Schmidt-Turkel scheme [45] in which the dispersive error is cancelled. It allows to reach the third-order space accuracy. The artificial viscosity includes a second-order dissipation term D_2 and a fourth-order dissipation term D_4, which involve two tunable parameters $k^{(2)}$ and $k^{(4)}$.
The viscous terms are discretized by a second-order space-centered scheme. For the turbulence transport equations, the upwind Roe scheme [46] is used to obtain a more robust method. The second-order accuracy is obtained by introducing a flux-limited dissipation [47].
Time integration is achieved using the dual time stepping approach and a low-cost implicit method consisting in solving, at each time step, a system of equations arising from the linearization of a fully implicit scheme. The derivative with respect to the physical time is discretized by a second-order formula.
The numerical treatment of boundary conditions is based on the use of the precon-

ditioned characteristic relationships. We assume that inlet and outlet areas are in a pure liquid region, no cavitation appears on these boundaries. An outlet pressure and an inlet velocity are specified, whereas a no slip condition is applied at the walls. More details are given in [23].

3. Experimental conditions and numerical set up

3.1. Experimental conditions [48]

The Venturi was tested in the cavitation tunnel of the CREMHyG (Centre d'Essais de Machines Hydrauliques de Grenoble). The test section is 520 mm long, 50 mm wide and 50 mm high in the inlet. It is characterized by a divergence angle of 4°, illustrated in Fig. 1. The edge forming the throat of the Venturi is used to fix the separation point of the cavity. This geometry is equipped with five probing holes to allow various measurements such as the local void ratio, instantaneous local speed and wall pressure (Fig. 1).

The selected operating point is characterized by the following physical parameters [48]:

$U_{inlet} = 10.8$ m/s, the inlet velocity

$\sigma_{inlet} = \dfrac{P_{inlet} - P_{vap}}{0.5\rho U_{inlet}^2} \simeq 0.55$, the cavitation parameter in the inlet section

$T_{ref} \simeq 293K$, the reference temperature

L_{ref}=252 mm, the reference length, which corresponds to the chord of a blade of a turbomachinery

$Re_{L_{ref}} = \dfrac{U_{inlet} L_{ref}}{\nu} = 2.7\,10^6$, the Reynolds number

With these parameters, a cavity length L ranging from 70 mm to 85 mm is obtained. The cavity is characterized by an almost constant length, although the closure re-

gion always fluctuates, with the presence of a re-entrant jet and little vapour cloud shedding. For this geometry, no periodic cycles with large shedding were observed.

3.2. Meshes

The initial 2D grid is a H-type topology. It contains 251 nodes in the flow direction and 62 nodes in the orthogonal direction. A special contraction of the mesh is applied in the main flow direction just after the throat to better simulate the two-phase flow area (Fig. 2). The y^+ values of the mesh, at the center of the first cell, vary between 12 and 27 for a non cavitating computation.

An investigation of the mesh influence, especially in the near-wall area, was performed in [43] for 2D Venturi cavitating flows. Results in good agreement with the experimental data were obtained with the considered 251×62 mesh.

From this grid, the 3D mesh was built by extruding the 2D mesh with 62 nodes in the cross direction z. As the test section is a square, the same grid evolution was applied in the y and z directions. A view of the mesh is presented in Figure 2. The y^+ values obtained from a non cavitating computation with the SA turbulence model vary between 1 and 20.

3.3. Numerical parameters

For the non cavitating regime, computations are started from a uniform flow-field using a local time step. For the unsteady cavitating regime, computations are performed with the dual time stepping method and are started from the cavitating numerical solution. The numerical parameters are:

- the dimensionless time step, $\Delta t^* = \dfrac{\Delta t U_{inlet}}{L_{ref}} = 4.9\,10^{-3}$
- number of sub-iterations for the dual time stepping method, 100
- the CFL number, 0.2

- Jacobi iterations for the implicit stage, 15

- the two coefficients of the artificial dissipation, $k^{(2)} = 1$ and $k^{(4)} = 0.045$ for the 2D computations and $k^{(4)} = 0.055$ for the 3D computations.

- the farfield value of the turbulent kinetic energy, $k_\infty = 0.0045$ m^2/s^2

- the farfield value of the turbulent length scale, $\ell_\infty = 1.4\,10^{-6}$ m

- the farfield value of the turbulent eddy-viscosity, $\mu_{t_\infty} = 10^{-4}$ Pa.s

4. Results

Six computations were performed (Tab 1): three on the 2D mesh and three on the 3D mesh.

For the DES computations, the value of the constant C_{DES} has been modified in order to capture a cavitation sheet behaviour in agreement with the experimental data. Consequently, the value is set to 0.9 instead of 0.65. The main reason to increase the value of the constant C_{DES} comes from the fact that with the standard value, the bottom wall just behind the throat is computed with the LES mode whereas with a value of $C_{DES} = 0.9$, the LES mode is moved a little bit away (Fig. 3). These small differences between the two computations are sufficient to transform the cavity. Indeed, with the standard value of C_{DES} only large cloud shedding are observed with no attached cavity at the throat.

First, a qualitative description of the 3D flow topology is displayed, followed by comparisons of local profiles between 2D and 3D computations. Finally, a special focus on the 3D solution obtained with the SA SAS model is presented with a study of velocity fluctuations and two-point correlations.

4.1. Qualitative description of the 3D computations

The Direct Fourier Transformation (DFT) of the vapour volume computed from the 3D computations put in evidence a low frequency (Tab.1), which is not observed with the 2D computations.

One way to explain such a behaviour can be provided from the results presented in [9] where a pulsating cavitation sheet on a NACA0015 hydrofoil is analysed using POD and DMD methods. It has been observed by several authors a bifurcation of shedding mechanism around the value $\frac{\sigma}{2\alpha} \approx 4$. For a lower value, the shedding mechanism would be driven by a shock wave, which propagates along the cavitation sheet closure. In this case, a low frequency associated with spanwise structures is observed. For an upper value, it is the re-entrant jet that controls the shedding mechanism and no low frequency is measured. For our Venturi test case, the value $\frac{\sigma}{2\alpha}$ is closed to 4, near the regime transition. Therefore a low frequency phenomenon can be expected. Furthermore, as it will be described below, this low frequency is associated with spanwise structures.

Figure 4 shows the density gradient modulus (Schlieren-like visualization) at different instants for the 3D computations. The throat of the Venturi is located at the abscissa $x = 0.002$ m. For the SAS computations, the low frequency is linked to a cross instability of the cavitation sheet. Indeed, the cavitation sheet growth is not homogeneous in the spanwise direction but alternates between the two lateral walls of the Venturi. In the case of the DES calculation, the sheet is more stable and presents a U shape form. Another way to view the shape of the cavity is to use an iso-surface of the void fraction. Figure 5 displays such an iso-surface for a value of the void fraction equal to 60%. Once again, the DES computation presents a cavity more stable compared to the SAS computations.

Downstream the cavitation sheet, the cross component w of the velocity field along

the bottom wall fluctuates at a low frequency and get value closed to 1 m/s (Fig.6), which corresponds 10% of the longitudinal velocity u.

Instantaneous snapshots of the void ratio and the velocity vector are plotted in Figure 7 in a transversal cutting plane at station 3 (abscissa $x = 0.0382$ m). For visualization convenience, the scale of the void fraction is widen to 1.5 but the value never exceeds 1. The velocity field in the cavitation sheet shows the presence of a vortical structure along the corner between the side wall and the bottom wall. The flow inside the cavity differs between DES and SAS computations. For the SAS computations, a transversal component is clearly present, which alternates at the same low frequency that the volume of vapour. For the DES computation, the velocity vector is vertical in the center of the Venturi and the cross component is quasi null. Near lateral walls, the cross component is present due to the corner vortex.

Consequently, the 3D computations makes appear 3D effects due to the presence of a cross flow component and a periodic fluctuation of the volume of vapour. For the SAS computations an oblique mode is exhibited corresponding to the alternated oscillation of the sheet in the spanwise direction. This phenomenon is not computed with the DES computation. To evaluate the impact of 3D effects on the mean flow in the mid-span section of the geometry, comparisons between 2D and 3D computations are proposed.

4.2. Comparisons between 2D and 3D computations

Comparisons between 2D and 3D simulations concern time-averaged quantities extracted on the mid-span plane: the longitudinal velocity u, the void fraction α, the pressure and the RMS pressure fluctuations at the wall. For the longitudinal velocity, the experimental value corresponds to the most probable one.

4.2.1. SAS computations

At station 1 (Fig.8), both the time-averaged velocity and void fraction are similar between 2D and 3D computations. At station 2, the $k-\ell$ SAS computation underestimates the void fraction due to the presence of a re-entrant jet along the bottom wall, which is not observed experimentally. At station 3 and 4, the void fraction predicted by the 3D computations is lower than in the 2D computations. About the velocity u, 3D computations do not have the same behaviour compared with 2D computations. The Spalart-Allmaras SAS 3D computation leads to a stronger and thicker re-circulation compared with the 2D computation, whereas the $k-\ell$ SAS 3D computation minimizes the re-circulation intensity compared with the 2D computation. Finally, at station 5, the SA SAS 3D computation does not predict void fraction, which is not the case for the 2D computation. For the $k-\ell$ SAS computations, 3D simulation provides a void fraction higher than the 2D solution.
The time-averaged wall pressure, plotted in Figure 9, does not evolved in the same way for the 3D computations. Indeed, the inlet cavitation number σ_{inlet} is higher for the 3D computations than the 2D computations, therefore, we expect that the mean wall pressure be higher for the 3D computations than the 2D ones. However, if this is the case for the computation with the Spalart-Allmaras SAS model, the opposite occurs with the $k-\ell$ SAS model.
The RMS wall pressure fluctuations (Fig.9) put in evidence large discrepancies between 2D and 3D computations. For the 2D computations, the peak of fluctuations is correctly located with an amplitude in agreement with the experimental measurements. Moreover, the decrease of the fluctuations level in the wake of the cavitation sheet is well captured. This is not the case for the 3D computations since the level of pressure fluctuations is largely overestimated in the wake.

4.2.2. DES computations

The time-averaged profiles for the void fraction and the longitudinal velocity are displayed in Figure 10. At the first two stations, the profiles are the same for the 2D and 3D calculations. At station 3, the 3D computation predicts a void fraction lower and a re-circulation slightly thicker than the 2D solution. At station 4, contrary to the 2D computation, the 3D calculation provides a void fraction and a longitudinal velocity close to the experimental one. Finally, at station 5, as previously observed with the SA SAS model, the 3D computation under-estimated the cavitation sheet length since no vapour is present at this station. This is linked to a smoother re-entrant jet in the 3D computation in comparison with the 2D case.

The time-averaged wall pressure profile and RMS fluctuations, plotted in Figure 11, show large discrepancy between the 2D and the 3D computations. The 3D computation under-estimates the wall pressure by a factor of three compared with the experiment and the 2D calculation. Similarly to SAS simulations, the RMS pressure fluctuations present a large value in the wake of the cavity for the 3D computation.

4.2.3. Partial conclusions

The time-averaged void fraction and velocity profiles show some small discrepancies between 2D and 3D computations particularly in the re-circulation area. Nevertheless, the re-entrant jet is well captured whatever the dimension of the domain. Moreover, a part of the difference can be explained by the fact that comparisons are done for different inlet cavitation numbers.

The wall pressure analysis put in evidence a 3D effect on the dynamic behaviour of the cavitation sheet. Mainly, the intensity of the pressure fluctuations are overestimated in the sheet as well as in the wake. Further reasons can be invoke to explain

these discrepancies between the 2D and 3D compuations. Firstly, the considered cavitation model (barotropic model) has never been tested in such 3D cavitating flows. It has been calibrated with 2D simulations. Maybe the link between the pressure and the density is too strong to simulate the 3D behaviour. Secondly, we assumed that the Boussinesq assumption is available with a relation between the mixture Reynolds tensor and the center of volume averaged velocity gradient. Maybe the assumptions are too strong in 3D cavitating flows. Additional experimental or numerical data are needed.

Therefore, 3D effects plays a role in the dynamic of the cavitation sheet even if both the velocity and void fraction profiles, where measurements are available, are not strongly affected. Indeed, it seems that 3D effects as we can see on the pressure fluctuations are essentially presented in the wake region located downstream the station of measurements. These effects manifest also by the low frequency pointed out on the vapour volume signal.

4.3. Analysis of the oblique mode

From the 3D computations performed with the Spalart-Allmaras SAS model, a global view of the dynamic of the cavitation sheet is displayed (statistical treatment on 2.2 seconds). Secondly, a deeper analysis is proposed with distributions and correlations in the mid-span section and a cross section (statistical treatment on 0.45 second only).

4.3.1. Global analysis

As shown before in Figure 4, the cavitation sheet is not symmetric in the spanwise direction and grows alternatively from one side of the Venturi to the other. The intensity of the cross flow is dampened away from the bottom wall, which confirms the role plays by the cavitation sheet in the formation of this flow. The structure of

the flow in the cavitation sheet is studied using a longitudinal cutting plane located at distance $y = 0.001$ m from the bottom wall. Six snapshots of the sheet are shown in Figure 12. The time between two snapshots is approximately $T_0 = \frac{T}{6} \approx 0.028$ second where T is the period of the oblique mode. The asymmetry of the cavitation sheet and the velocity field are well exhibited. At $t = 0$, the sheet is asymmetric with an attached cavity (defined by a void fraction higher than 0.9) expands to $x = 0.06$ m on the side $z = 0.05$m and only to $x = 0.03$ m on the other side. At the center of the Venturi, the re-entrant jet develops more upstream than at the walls. The presence of the side walls can explain such a behaviour. Firstly, for the flow upstream the Venturi throat, the sheet is equivalent to an obstacle. To by-pass this obstacle, two possibilities are offered to it: to pass over the cavity or to pass along the side walls. Forcing the pass leads to an acceleration of the flow (Fig.13) confined between the cavitation sheet and the wall, which plays the role of a small local venturi. Consequently, the momentum energy of the flow is increased, allowing it to better resist to the re-entrant jet. Secondly, the side walls involve the formation of corner vortices (Fig.7), which deflect the re-entrant jet to the center. Therefore, the re-entrant momentum energy is enforced at the center, which allows it to develop deeper.

At $t = \frac{T_0}{6}$, the re-entrant jet leads to the cavity decrease along the side $z = 0.05$m whereas the cavitation sheet is growing along the opposite wall. At $t = \frac{2T_0}{6}$, the re-entrant jet on the side $z = 0.05$m is deflected to the center of the Venturi. On the other side, the cavitation sheet follows its growth. At $t = \frac{3T_0}{6}$, the cavitation sheet reaches its maximum length on the side $z = 0$ and a liquid re-entrant jet appears. On the opposite side, the vortex corner begins to expand, taking with it the sheet. At $t = \frac{4T_0}{6}$, the re-entrant jet along the side $z = 0$ makes face to the vortex corner and is deflected to the center. Along the other side, the cavitation sheet lengthens. At

$t = \frac{5T_0}{6}$, the re-entrant jet on the side $z = 0$ flows to the center of the Venturi, while on the opposite side no re-entrant jet is observed and the cavitation sheet reaches its maximum length.

Figure 13 shows the time-averaged velocity and void ratio evolutions in the spanwise direction at different abscissa ($x = 0.0083$ m and $x = 0.02$ m inside the attached cavity and $x = 0.027$ m at the end of the attached cavity). The void fraction increases along the side walls due to the fact that the corner vortex sucks a part of stable cavity, which has to make faced to the re-entrant jet.

4.3.2. Analysis in the mid-span section

The analysis focuses on both the longitudinal and cross components of the velocity. Except for the longitudinal velocity, no comparisons can be done with the experiments.

In the experimental data, due the non gaussian distribution of the longitudinal velocity inside the cavitation sheet, the most probable values were chosen for the longitudinal velocity profiles instead of time-averaged values. In order to verify the capability of computations to capture a part of this non gaussian distribution, we extracted the distributions of the resolved fluctuating part of both the longitudinal and cross velocities at all measurement stations. These distributions are plotted in Figures 14 and 15 at stations 3 to 5. Four altitudes are selected: one in the re-circulation area ($y = 0.7$ mm), two in the shear stress layer ($y = 2$ mm and $y = 4$ mm) and one out of the cavitation sheet ($y = 8.5$ mm). The distribution of the velocities is closed to be gaussian at station 5 and for all the stations at the distance $y = 8.5$ mm. On the other hand, in the cavitation sheet, the distribution are not gaussian and displayed a large interval of probable values. For instance, the distribution of the longitudinal velocity at station 3 and at the distance $y = 4$ mm from the bottom wall shows a

plateau of probable values from 6 to 11 m/s. For the cross velocity, the large discrepancy between the probable value makes appear often two peaks: one located in the negative values and the other located in the positive values. This observation is correlated with the cross instability mentioned above.
The RMS velocity fluctuations and the comparison between mean and most probable values are illustrated in Figure 16 for the five stations of measurement. At stations 1 and 2, the mean and the most probable longitudinal velocity profiles are closed one to each other. The RMS values of the resolved part of the velocity field are of the same order of magnitude in each direction, which means that the turbulence is isotropic. From stations 3 to 5, the velocity field shows a non gaussian behaviour. Indeed, the mean and most probable profiles differ particularly in the shear stress region. For instance, at station 3, the gap between the most probable and the mean value can reach 2 m/s. For the RMS velocity fluctuations, the fluctuations in the longitudinal direction are largely higher in comparison with values in the orthogonal and cross directions. At station 3, the ratio u_{rms}/v_{rms} can be close to 10. Therefore, the turbulence can not be considered as isotropic in the re-circulating area. At station 5, the gap between the most probable value and the mean value reduces and the fluctuation comes back to an isotropic behaviour.

To conclude, the analysis in the mid-span section put in evidence that the velocity field is not gaussian in the re-circulation area and the turbulence at large-scales can not be considered as isotropic. Out of the re-circulation area, the velocity field is gaussian and the large-scales turbulence is isotropic.

4.3.3. Analysis in a transversal cutting plane

The analysis in a transversal cutting plane located at station 3 (abscissa $x = 38$ mm) inside the re-circulation zone is proposed. Three instantaneous snapshots of the void ratio and the velocity vector are depicted in Figure 17. Only an enlargement near the side $z = 0$ is presented. For these pictures, the scale of the void ratio is greater than 1 to improve the contrast of visualizations. A preliminary portrait of the flow can be derived. Firstly, the corner vortex is 5 mm large and seems to be weakly affected by the cross flow. These vortices play two roles: in one hand, they capture a part of the outer flow and feed the sheet in vapour, on the other hand, they deflect the liquid re-entrant jet to the center of the Venturi. Secondly, the cross flow is located in the re-circulation area whereas out of the cavitation sheet, the velocity vectors do not show a global alignment with a strong intensity. Therefore, the shear stress induced by the re-entrant jet leads to a de-correlation of the flow between the cavitation sheet and the outer flow.

Spatial two-point correlations based on the void fraction and the longitudinal and cross velocities have been calculated along the span. Three different distances from the bottom wall have been considered: $y = 5$ mm, $y = 6.4$ mm and $y = 7.2$ mm. Along the spanwise, three different points have been chosen in order to verify the width on which the flow can be considered to be two-dimensional. The considered reference points are located at the third, the half and the two-third of the span, respectively. These correlations are presented in Figure 18. For the extreme points, the longitudinal velocity and void fraction correlations are very low compared with the cross velocity correlation. Therefore, we conclude that the re-entrant jet is not coherent in the cavitation sheet and the cross flow is a motion over all the span. At mid-span, correlations show that the re-entrant jet is correlated over a distance of

5 mm on each side of the mid-point. Over this distance, the correlations decrease, which is not the case for the cross velocity. Once more, the cross velocity shows only a slight decrease of the correlation over the span (excepted at the distance $y = 6.4$ mm) that confirms the presence of a global cross motion in the cavitation sheet.
Correlations between the two lateral sides have been also evaluated for the longitudinal velocity and the void ratio. The temporal evolution is presented in Figure 19. It is noticeable that the void fraction and the longitudinal velocity correlations superimpose. Therefore, the re-entrant jet and the evolution of the cavity are linked one to each other. The analysis of the correlated signal put in evidence the low frequency of 6 Hz and a phase difference close to π and confirms that the cavitation sheet evolves in an opposite phase between the two sides of the Venturi.

5. Conclusion

In the present study, 2D and 3D computations of a cavitation sheet developing along the bottom wall of a Venturi geometry have been performed using the DES approach and Scale-Adaptive models. The DES model has undergone a modification of the constant C_{DES} since the standard value was replaced by 0.9, which allowed to capture a cavitation sheet behaviour in agreement with the experimental one.
First, comparisons between 2D and 3D (in the mid-span section) computations were presented together with the experimental results. The mean void fraction and the mean longitudinal velocity profile exhibited very small discrepancies between the 2D and the 3D computations. On the contrary, the mean pressure profile and the RMS pressure fluctuations at the bottom wall put in evidence large differences between 2D and 3D computations. Overall, 3D computations tend to underestimate the pressure in the wake of the cavitation sheet, whereas the RMS pressure fluctuations are overestimated in the cavitation sheet and in the wake. Indeed, downstream the cavitation

sheet, the 3D computations provide a plateau of RMS pressure fluctuations, which is not observed experimentally or computed by the 2D simulations. The dynamic behaviour of the cavitation sheet changes between the 2D and 3D computations.

The 3D computations were analyzed in more details. A cross instability at low frequency (around 6 Hz) was illustrated corresponding to a cross flow inside the re-circulation area and leading to a growth of the cavitation sheet in an opposite phase between the two Venturi sides. This results are in agreement with recent observations provided by an experimental study of a pulsating cavitation sheet over a NACA0015 hydrofoil [9]. From the numerical computations, the main reason to explain this phenomenon comes from the presence of a vortex at each side of the Venturi, which modify the structure of the cavitation sheet. These vortices suck a part of the flow allowing a larger growth of the cavity and deflects the re-entrant jet to the center of the geometry. It was observed that the thickness of the vortex was almost constant in time and close to 5 mm. The cross flow takes place in all the re-circulation area as it is confirmed by the high level of the spanwise velocity correlations through the cavitation sheet. On the contrary, the re-entrant jet is not uniform in the spanwise direction but only in a section laying from $z = 0.02$ m to $z = 0.03$ m.

On the other hand, the analysis of the longitudinal and spanwise velocity distributions made appear a turbulent flow that is not isotropic and gaussian in the re-circulation zone. Consequently, the most probable value of the longitudinal velocity differs from the mean value and the RMS fluctuations of the resolved longitudinal velocity are larger than the other components.

From this investigation, 3D effects are suggested through the presence of corner vortices and a cross instability. Moreover, a non canonical turbulent flow is shown in the re-circulation zone, which can be an explanation for the inability of the standard turbulence models to capture the unsteady behaviour of the cavitation sheet. Even

if the pressure fluctuations obtained with the 3D computations are less accurate, several lessons can be drawn:

- enhanced turbulence models are needed to capture the behaviour of unsteady cavities (particularly the re-entrant jet),
- side-wall effects have an major influence on the cavity growth and the flow downstream the cavity,
- the investigation of the sheet dynamics can not restrain itself to the evaluation of mean quantities and has to focus on resolved fluctuations.

Finally, additional experimental measurements or computations will be welcome to attest the presented results and to better understand the phenomenon.

Acknowledgement

The authors wish to thank the IDRIS - CNRS supercomputing center for providing us their computing resources.

References

[1] K. Laberteaux, S. Ceccio, Partial cavity flows. Part1. Cavities forming on models without spanwise variation, Journal of Fluid Mechanics 431 (2001) 1–41.

[2] D. de Lange, G. Bruin, L. van Wijngaarden, On the mechanism of cloud cavitation - experiments and modelling, in: 2nd International Symposium on Cavitation CAV1994, Tokyo, Japan, 1994.

[3] Y. Kawanami, H. Kato, H. Yamaguchi, M. Tanimura, Y. Tagaya, Mechanism and control of cloud cavitation, Journal of Fluids Engineering 119 (4) (1997) 788–794.

[4] G. Reisman, Y.-C. Wang, C. Brennen, Observations of shock waves in cloud cavitation, Journal of Fluid Mechanics 355 (1998) 255–283.

[5] S. Gopalan, J. Katz, Flow structure and modeling issues in the closure region of attached cavitation, Physics of Fluids 12 (4) (2000) 895–911.

[6] D. de Lange, G. de Bruin, Sheet cavitation and cloud cavitation, re-entrant jet and three-dimensionality, Applied Scientific Research (1998) 91–114.

[7] K. Laberteaux, S. Ceccio, Partial cavity flows. Part2. Cavities forming on test objects with spanwise variation, Journal of Fluid Mechanics 431 (2001) 43–63.

[8] E. Foeth, C. van Doorne, T. van Terwisga, B. Wienecke, Time-resolved PIV and flow visualization of 3D sheet cavitation, Experiments in Fluids 40 (2006) 503–513.

[9] S. Prothin, J.-Y. Billard, H. Djeridi, Image processing using POD and DMD for the study of cavitation development on a NACA0015, in: 13th Journées de l'Hydrodynamique, Laboratoire Saint-Venant, Chatou, France, 2012.

[10] G. Schnerr, I. Sezal, S. Schmidt, Numerical investigation of three-dimensional cloud cavitation with special emphasis on collapse induced shock dynamics, Physics of Fluids 20 (2008) 040703.

[11] A. Koop, H. Hoeijmakers, Unsteady sheet cavitation on three-dimensional hydrofoil, in: 7^{th} International Conference on Multiphase Flow, Tampa, USA, 2010.

[12] S. Park, S. Hyung Rhee, Numerical analysis of the three-dimensional cloud cavitating flow around a twisted hydrofoil, Fluid Dynamics Research 45 (1) (2013) 1–20.

[13] G. Wang, M. Ostoja-Starzewski, Large eddy simulation of a sheet/cloud cavitation on a NACA0015 hydrofoil, Applied Mathematical Modeling 31 (2007) 417–447.

[14] N. Dittakavi, A. Chunekar, S. Frankel, Large eddy simulation of turbulent-cavitation interactions in a Venturi nozzle, Journal of Fluids Engineering 132 (12) (2010) 121301.

[15] R. Bensow, G. Bark, Simulating cavitating flows with LES in openfoam, in: V ECCOMAS CFD, Lisbon, Portugal, June 2010.

[16] N.-X. Lu, R. Bensow, G. Bark, LES of unsteady cavitation on the Delft twisted foil, Journal of Hydrodynamics, serie B 22 (5) (2010) 784–790.

[17] P. Spalart, Detached-eddy simulation, Annual Review of Fluid Mechanics 41 (2009) 181–202.

[18] R. Kunz, J. Lindau, T. Kaday, L. Peltier, Unsteady RANS and detached-eddy simulations of cavitating flow over a hydrofoil, in: 5^{rd} International Symposium on Cavitation CAV2003, Osaka, Japan, 2003.

[19] M. Kinzel, J. Lindau, L. Peltier, R. Kunz, S. Venkateswaran, Detached-eddy simulations for cavitating flows, in: AIAA-2007-4098, $18^{t}h$ AIAA Computational Fluid dynamics Conference, Miami, USA, 2007.

[20] R. Bensow, Simulation of the unsteady cavitation on the Delft twist11 foil using RANS, DES and LES, in: Second International Symposium on Marine Propulsors, Hamburg, Germany, June 2011.

[21] B. Ji, X. Luo, X. Peng, H. Xu, Partially-averaged Navier-Stokes method with modified $k - \varepsilon$ model for cavitating flow around a marine propeller in a non-uniform wake, Int. Journal of Heat and Mass Transfer 55 (2012) 6582–6588.

[22] B. Ji, X. Luo, Y. Wu, X. Peng, Y. Duan, Numerical analysis of unsteady cavitating turbulent flow and shedding horse-shoe vortex structure around a twisted hydrofoil, International Journal of Multiphase Flow 51 (2013) 33–43.

[23] E. Goncalves, R. F. Patella, Numerical simulation of cavitating flows with homogeneous models, Computers & Fluids 38 (9) (2009) 1682–1696.

[24] E. Goncalves, Numerical study of unsteady turbulent cavitating flows, European Journal of Mechanics B/Fluids 30 (1) (2011) 26–40.

[25] J. Decaix, E. Goncalves, Time-dependent simulation of cavitating flow with $k-\ell$ turbulence models, Int. Journal for Numerical Methods in Fluids 68 (2012) 1053–1072.

[26] F. Menter, The scale-adaptive simulation method for unsteady turbulent flow predictions. Part 1: Theory and model description, Flow, Turbulence and Combustion 85 (1) (2010) 113–138.

[27] C. Ishii, T. Hibiki, Thermo-fluid dynamics of two-phase flow, Springer (2006).

[28] Y. Delannoy, J. Kueny, Two phase flow approach in unsteady cavitation modelling, in: Cavitation and Multiphase Flow Forum, ASME-FED, vol. 98, pp.153-158, 1990.

[29] H. Guillard, C. Viozat, On the behaviour of upwind schemes in the low Mach number limit, Computers & Fluids 28 (1) (1999) 63–86.

[30] E. Turkel, Preconditioned methods for solving the incompressible and low speed compressible equations, Journal of Computational Physics 172 (2) (1987) 277–298.

[31] J.-L. Reboud, B. Stutz, O. Coutier, Two-phase flow structure of cavitation: experiment and modelling of unsteady effects, in: 3^{rd} International Symposium on Cavitation CAV1998, Grenoble, France, 1998.

[32] O. Coutier-Delgosha, J. Reboud, Y. Delannoy, Numerical simulation of the unsteady behaviour of cavitating flow, Int. Journal for Numerical Methods in Fluids 42 (2003) 527–548.

[33] Y. Chen, C. Lu, L. Wu, Modelling and computation of unsteady turbulent cavitation flows, Journal of Hydrodynamics 18 (5) (2006) 559–566.

[34] L. Zhou, Z. Wang, Numerical simulation of cavitation around a hydrofoil and evaluation of a RNG $k-\varepsilon$ model, Journal of Fluid Engineering 130 (1) (2008) 011302.

[35] P. Spalart, W. Jou, M. Strelets, S. Allmaras, Comments on the feasibility of LES for wings and on hybrid RANS//LES approach, in: 1st AFSOR Int. Conf. on DNS/LES - Ruston, 1997.

[36] P. Spalart, S. Deck, M. Shur, K. Squires, M. Strelets, A. Travin, A new version of detached-eddy simulation, resistant to ambiguous grid densities, Theoretical Computational Dynamics 20 (2006) 181–195.

[37] F. Menter, Y. Egorov, A scale-adaptive simulation model using two-equation models, in: AIAA 2005–1095, 43rd Aerospace Science Meeting and Exhibit, Reno, Nevada, 2006.

[38] J. Rotta, Turbulente Strmumgen, BG Teubner Stuttgart, 1972.

[39] F. Menter, The scale-adaptive simulation method for unsteady turbulent flow predictions. Part 2: Application to complex flows, Flow, Turbulence and Combustion 85 (1) (2010) 139–165.

[40] L. Davidson, Evaluation of the SST-SAS model: channel flow, asymmetric diffuser and axi-symmetric hill, in: Proceedings of ECCOMAS CFD 2006, Egmond aan Zee, The Netherlands, 2006.

[41] B. Smith, The $k-kl$ turbulence model and wall layer model for compressible flows, in: AIAA 90–1483, 21^{st} Fluid and Plasma Dynamics Conference – Seattle, Washington, 1990.

[42] F. Menter, Eddy viscosity transport equations and their relation to the $k - \epsilon$ model, Journal of Fluids Engineering 119 (1997) 876–884.

[43] E. Goncalves, J. Decaix, Wall model and mesh influence study for partial cavities, European Journal of Mechanics B/Fluids 31 (1) (2012) 12–29.

[44] J. Viegas, M. Rubesin, Wall–function boundary conditions in the solution of the Navier–Stokes equations for complex compressible flows, in: AIAA 83–1694, 16^{th} Fluid and Plasma Dynamics Conference – Danver, Massachussetts, 1983.

[45] A. Jameson, W. Schmidt, E. Turkel, Numerical solution of the Euler equations by finite volume methods using Runge-Kutta time stepping schemes, in: AIAA Paper 81–1259, 1981.

[46] P. Roe, Approximate Riemann solvers, parameters vectors, and difference schemes, Journal of Computational Physics 43 (1981) 357–372.

[47] S. Tatsumi, L. Martinelli, A. Jameson, Flux-limited schemes for the compressible Navier-Stokes equations, AIAA Journal 33 (2) (1995) 252–261.

[48] S. Barre, J. Rolland, G. Boitel, E. Goncalves, R. F. Patella, Experiments and modelling of cavitating flows in Venturi: attached sheet cavitation, European Journal of Mechanics B/Fluids 28 (2009) 444–464.

Table 1: Numerical computations.

Turbulence model	Dimension of the domain	σ_{inlet}	Frequency (Hz)
$k-\ell$ SAS	2D	0.580	no particular frequency
$k-\ell$ SAS	3D	0.590	≈ 6
SA-SAS	2D	0.588	no particular frequency
SA-SAS	3D	0.6	≈ 6
SA-DES	2D	0.588	no particular frequency
SA-DES	3D	0.6	≈ 3

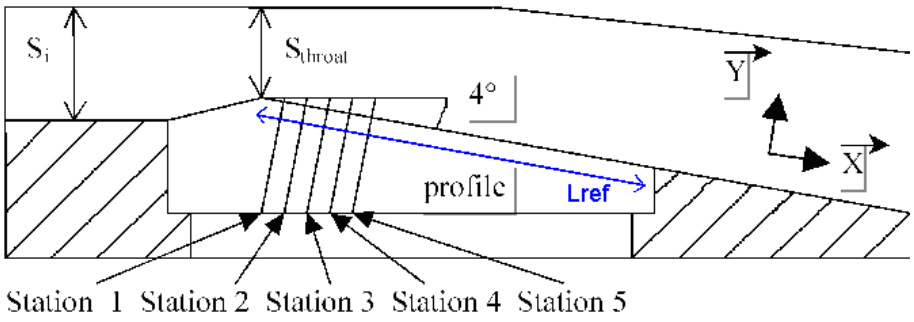

Figure 1: Schematic view of the 4° Venturi profile.

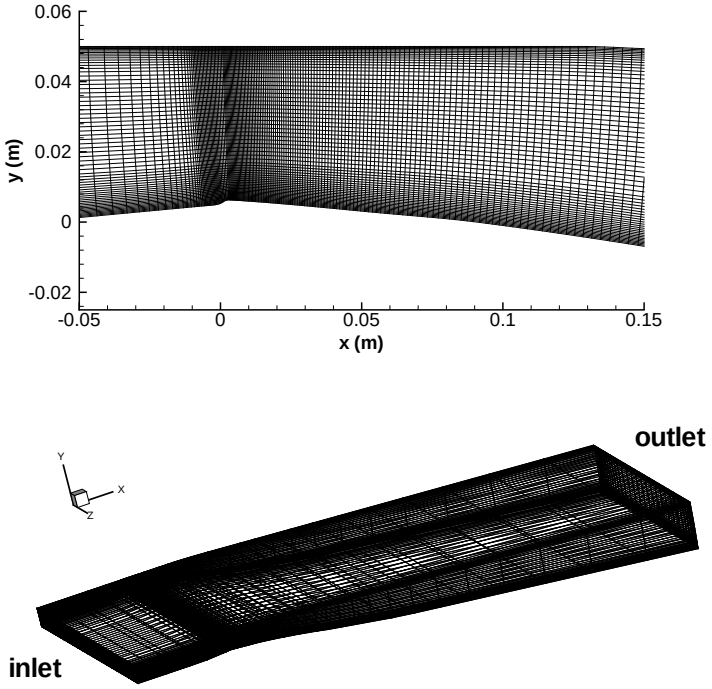

Figure 2: View of the 2D mesh near the Venturi throat and view of the 3D mesh.

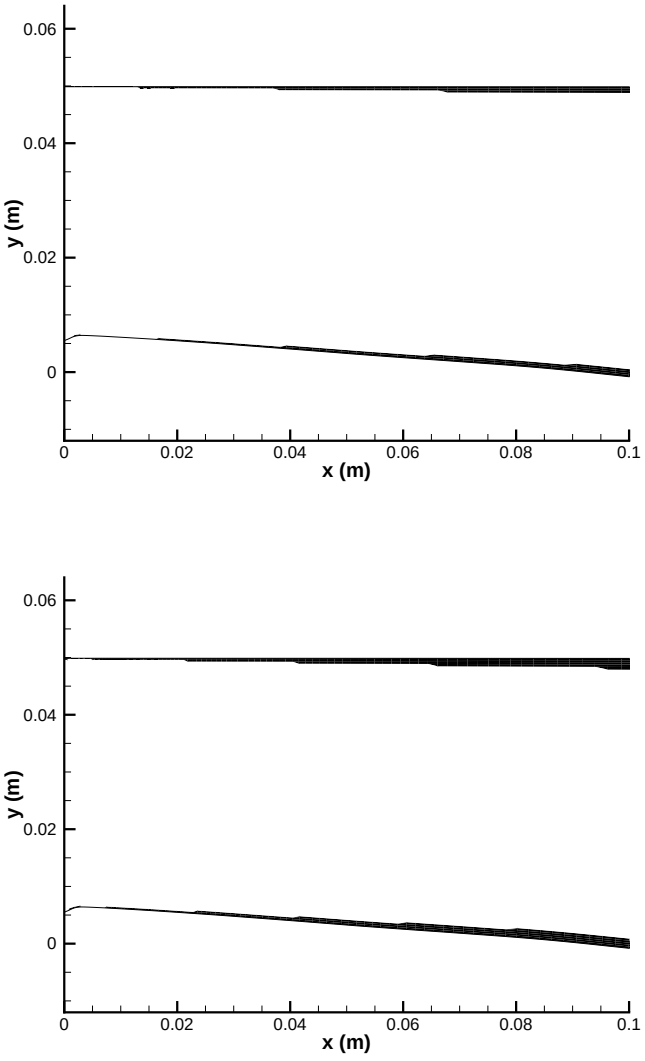

Figure 3: View of the RANS (black) ans LES (white) regions in the mid-span section for the DES computations with $C_{DES} = 0.65$ (top) and $C_{DES} = 0.9$ (bottom).

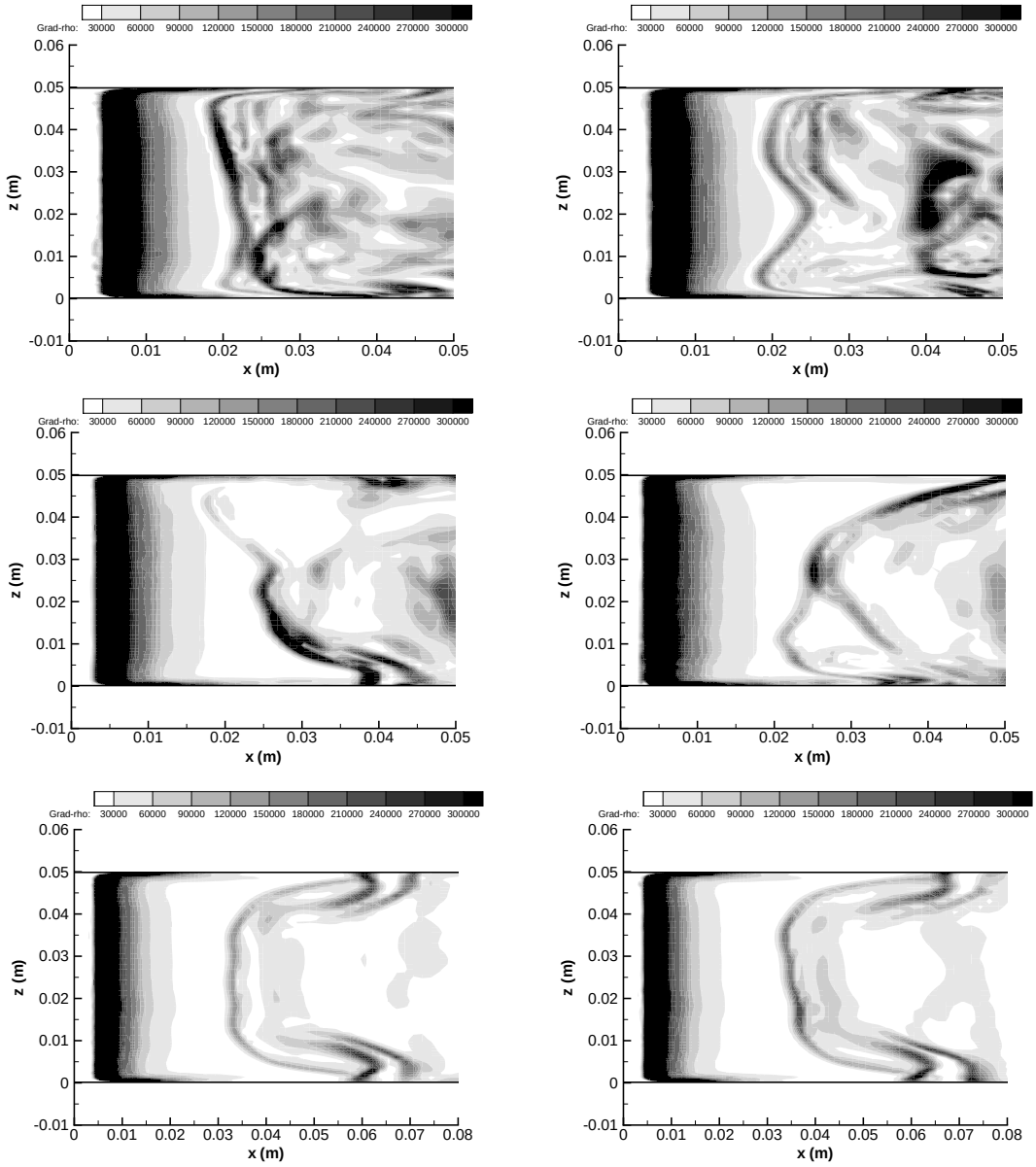

Figure 4: Gradient density modulus visualization at two different instants: $k-\ell$ SAS (top), Spalart-Allmaras SAS (middle) and DES (bottom), 3D computations.

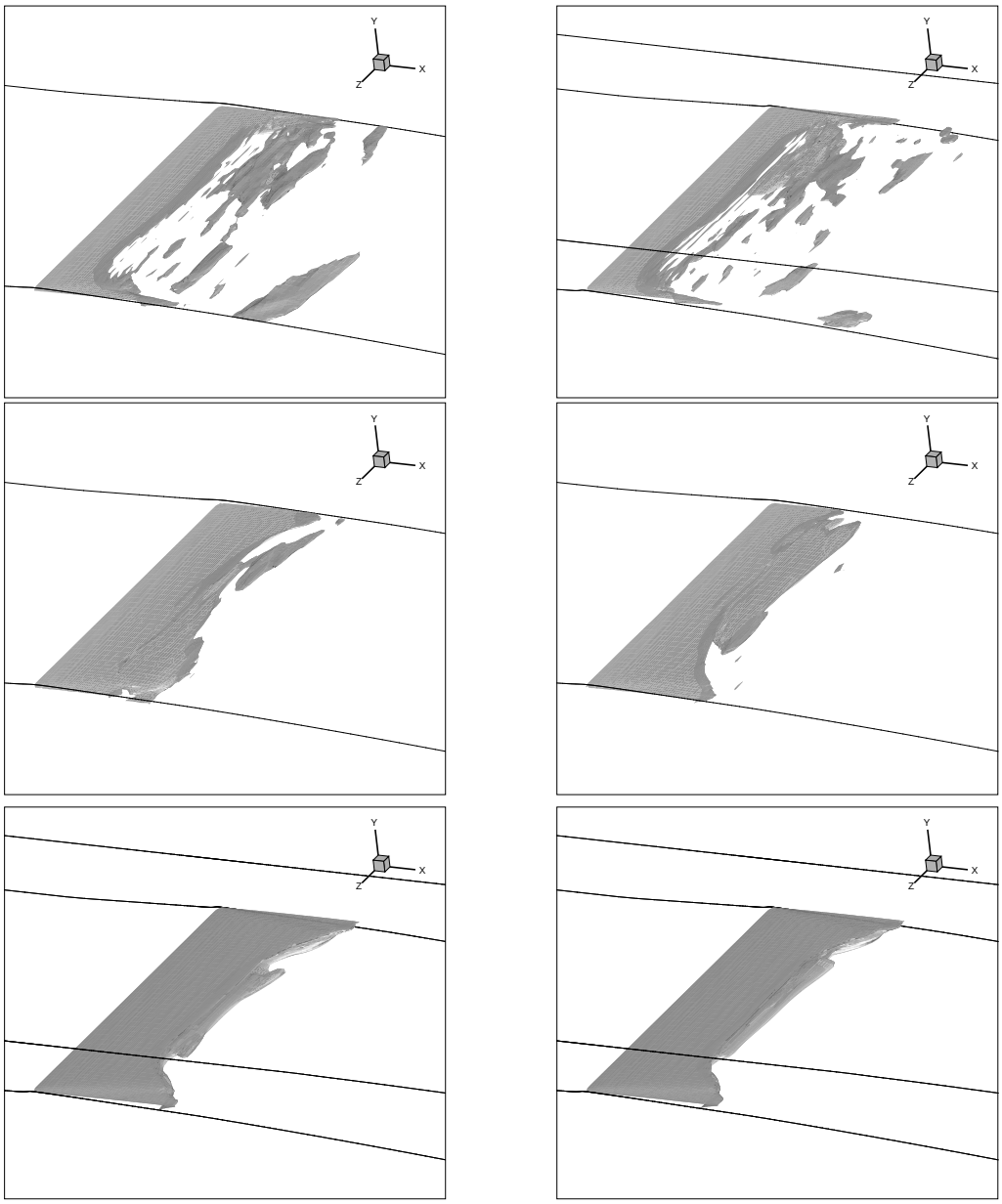

Figure 5: Iso-surface of the void fraction for the value of 60% at two different instants: $k - \ell$ SAS (top), Spalart-Allmaras SAS (middle) and DES (bottom), 3D computations.

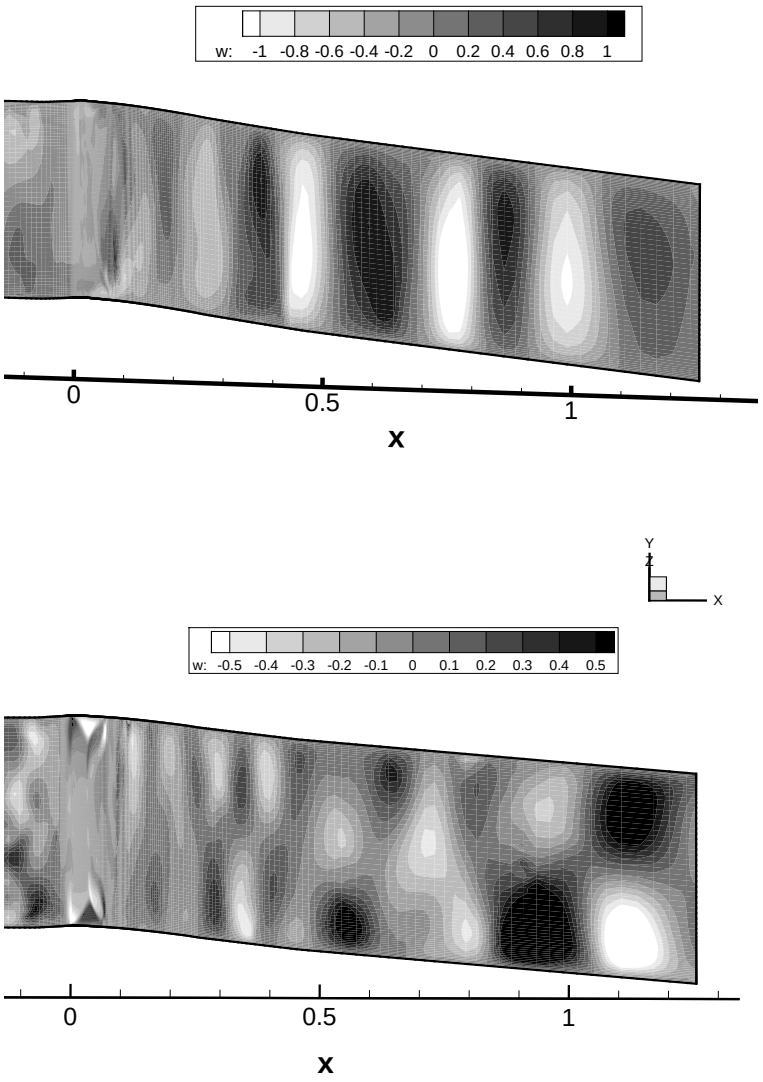

Figure 6: Transversal component w of velocity field, SA-SAS (top) and SA-DES (bottom) located at 10^{-3} m from the bottom wall.

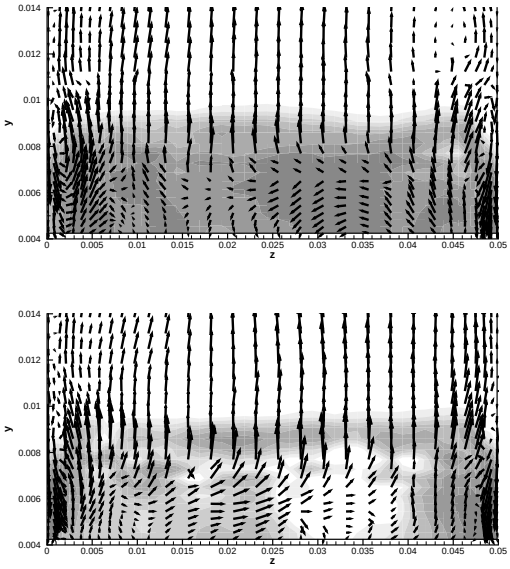

$k - \ell$ SAS simulation

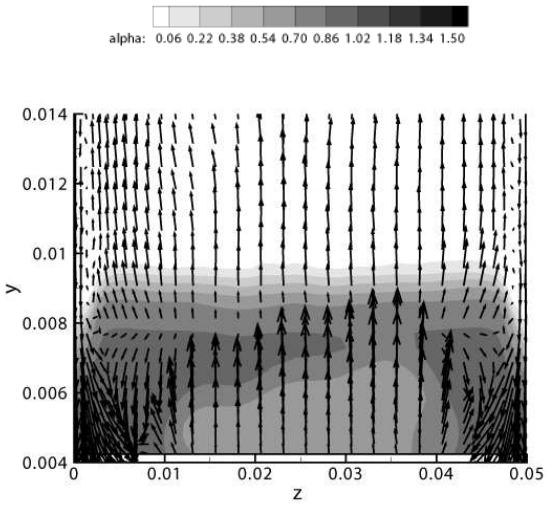

SA DES simulation

Figure 7: Void fraction and velocity vector at two different instants in a transversal cutting plane at station 3, $k - \ell$ SAS (left) and SA-DES (right).

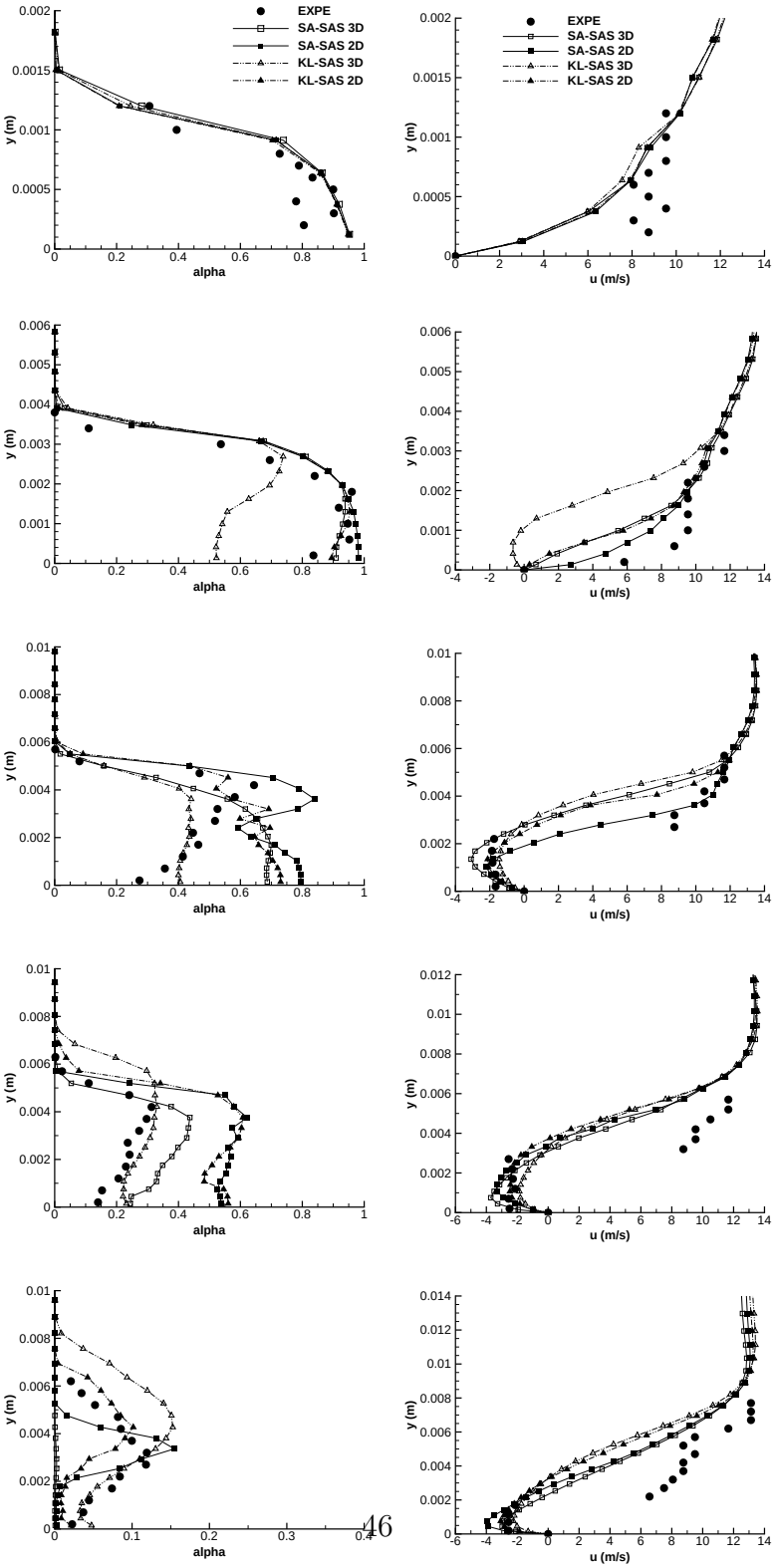

Figure 8: Time-averaged void fraction (left) and longitudinal velocity (right) profiles from station 1 (top) to 5 (bottom), SAS computations.

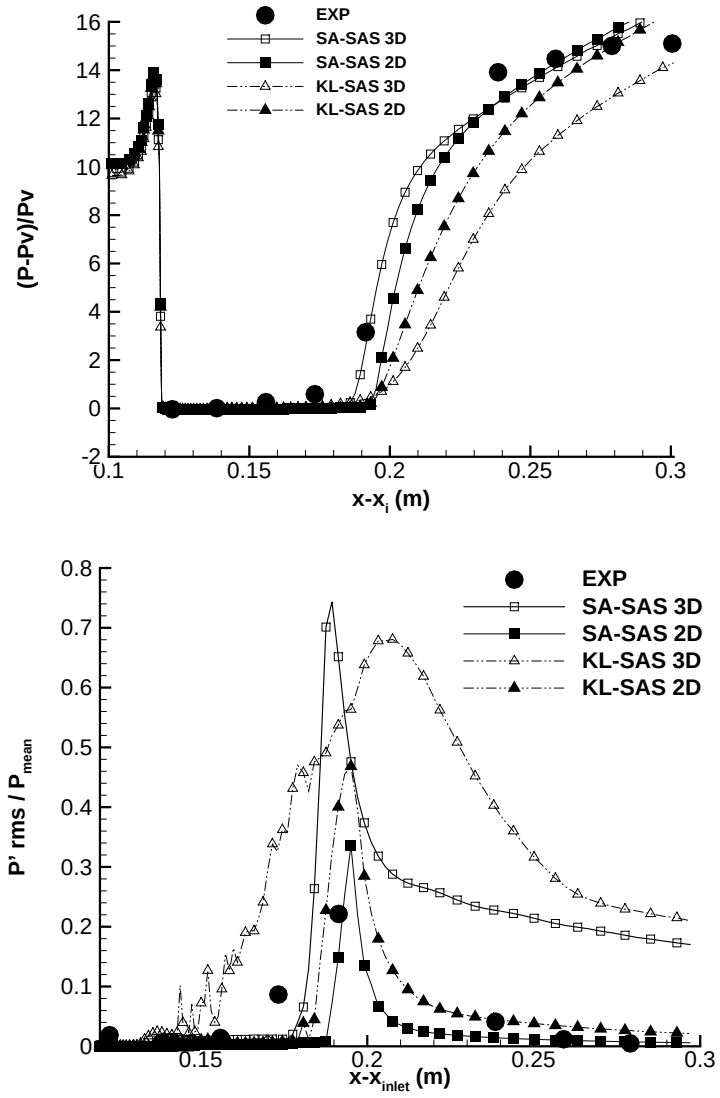

Figure 9: Time-averaged wall pressure (top) and RMS fluctuations (bottom) along the bottom wall, SAS computations.

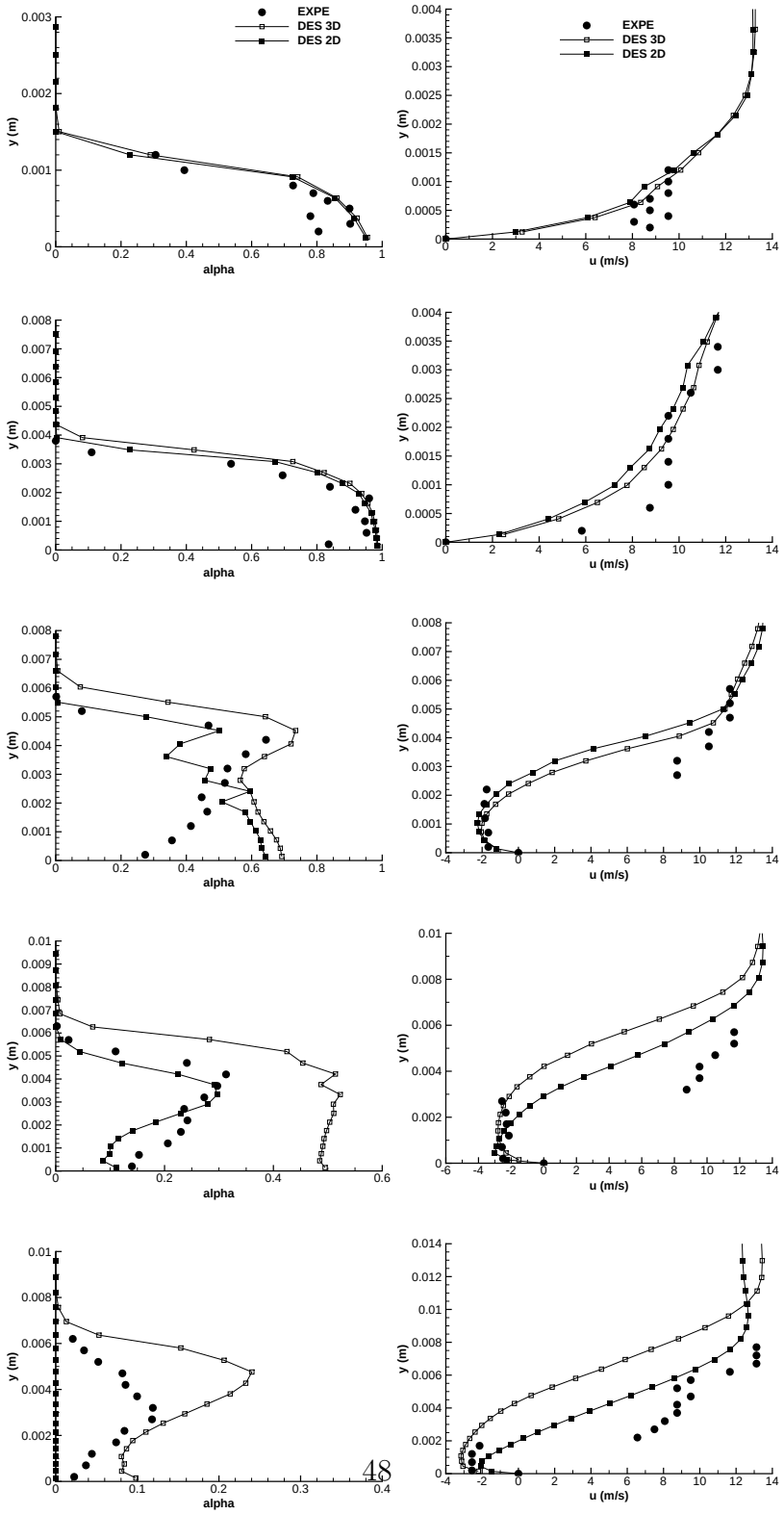

Figure 10: Time-averaged void fraction (left) and longitudinal velocity (right) profiles from station 1 (top) to 5 (bottom), DES computations.

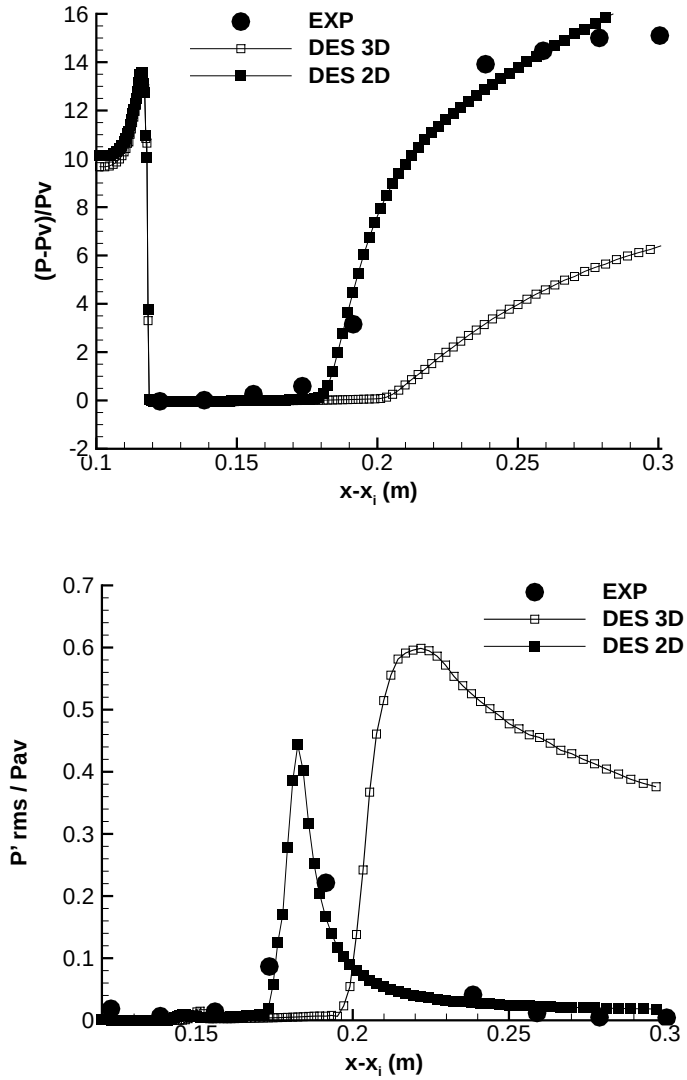

Figure 11: Time-averaged wall pressure (top) and RMS fluctuations (bottom) along the bottom wall, DES computations.

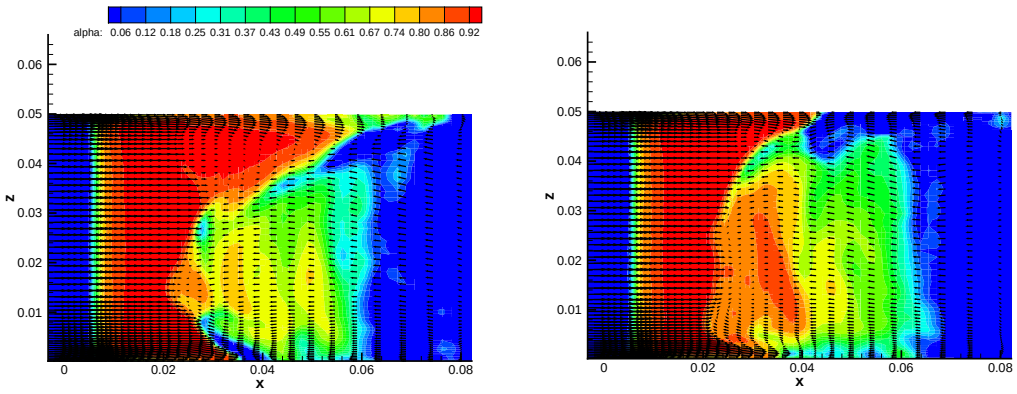

$t = 0$ $t = T_0$

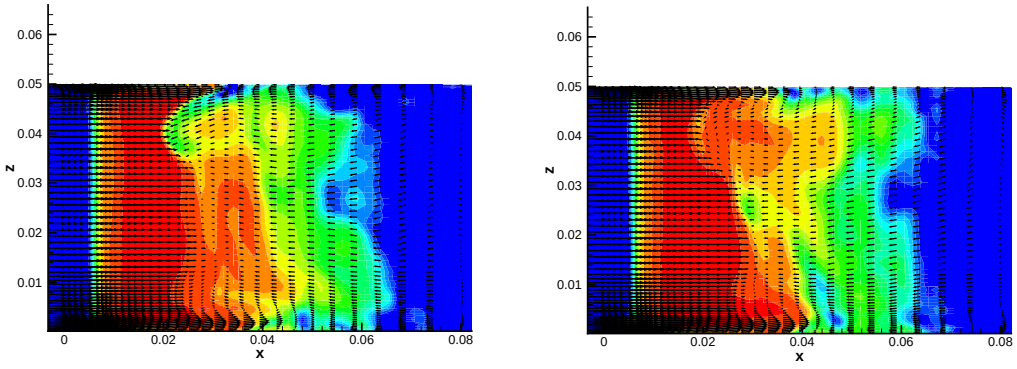

$t = 2T_0$ $t = 3T_0$

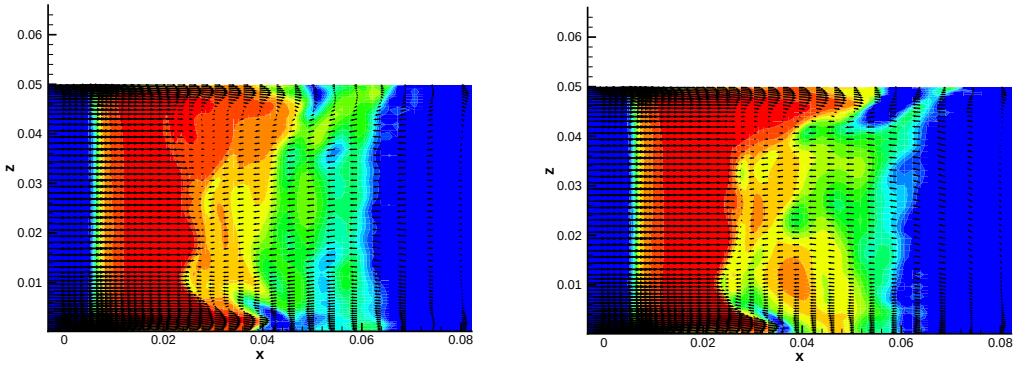

$t = 4T_0$ $t = 5T_0$

Figure 12: Void fraction and velocity vector at six different instants, in a cutting plane located at $y = 10^{-3}$ m.

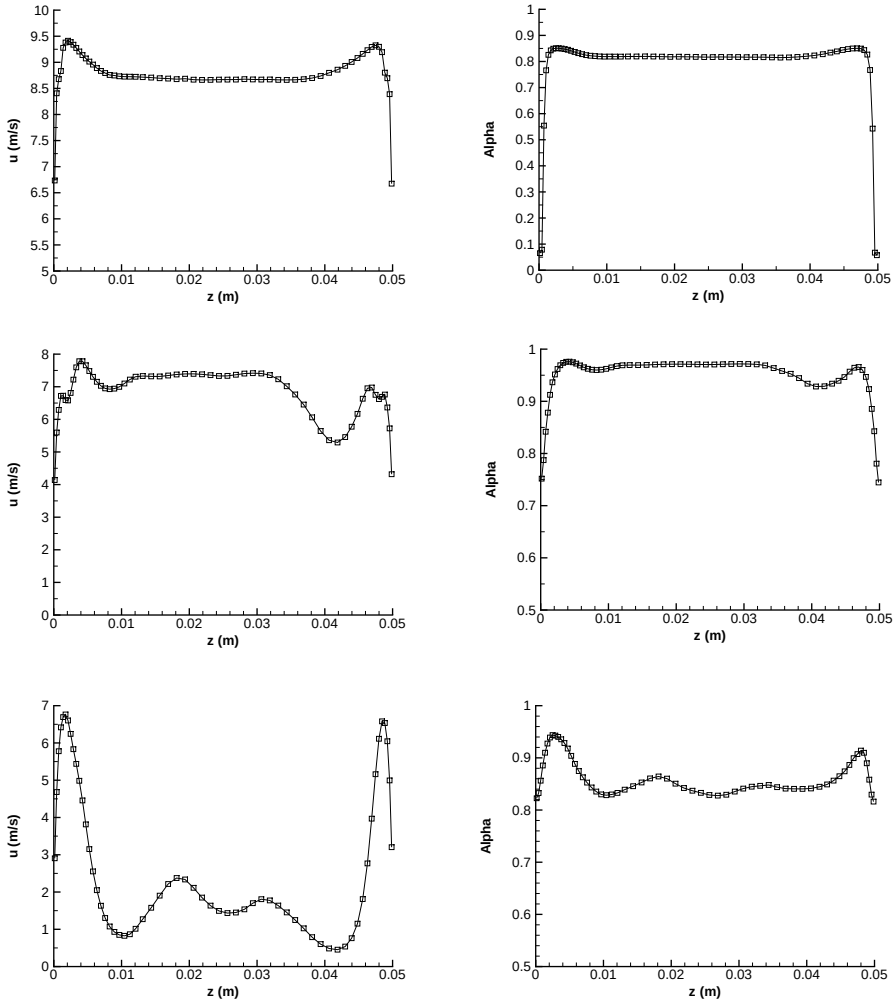

velocity component u void ratio α

Figure 13: Time-averaged longitudinal velocity (left) and void fraction (right) profiles in the span direction at distance $y = 10^{-3}$ m and abscissa $x = 8.3\,10^{-3}$ m (top) ; $x = 2\,10^{-2}$ m (middle) and $x = 2.7\,10^{-2}$ m (bottom).

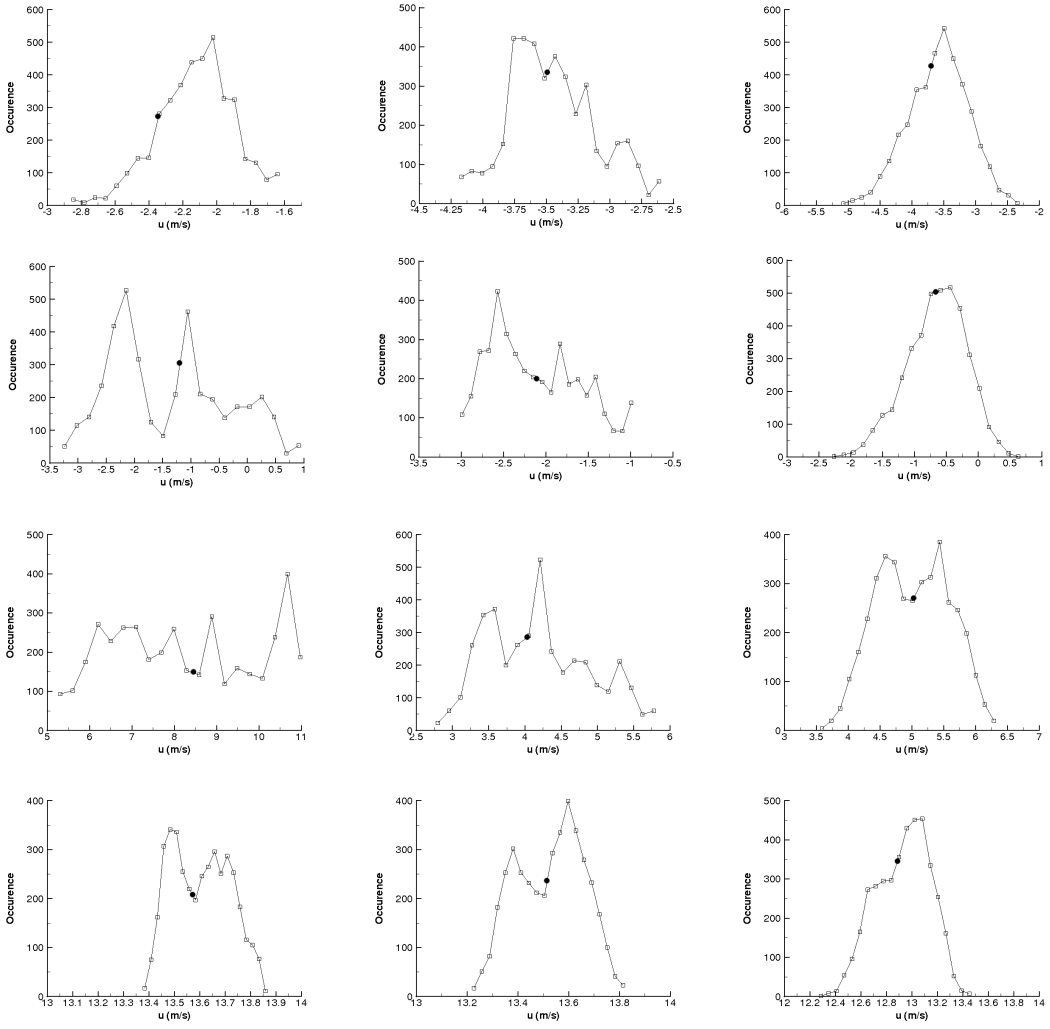

station 3 station 4 station 5

Figure 14: Distribution of the longitudinal velocity u from station 3 to 5 (left to right) at four distances from the bottom wall: $y = 0.7$ mm ; $y = 2$ mm ; $y = 4$ mm and $y = 8.5$ mm (top to bottom). (•) refers to the mean value.

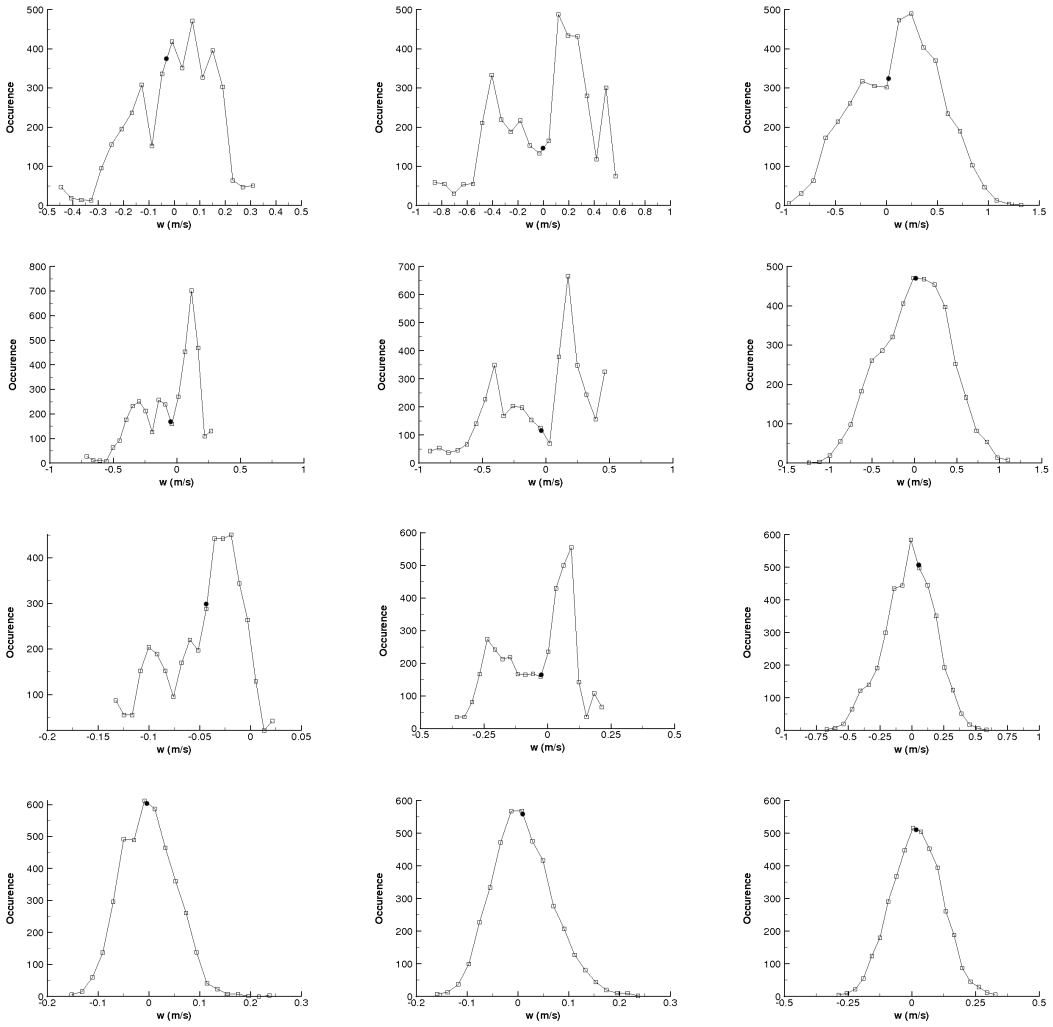

station 3 station 4 station 5

Figure 15: Distribution of the transversal velocity w from station 3 to 5 (left to right) at four distances from the bottom wall: $y = 0.7$ mm ; $y = 2$ mm ; $y = 4$ mm and $y = 8.5$ mm (top to bottom). (•) refers to the mean value.

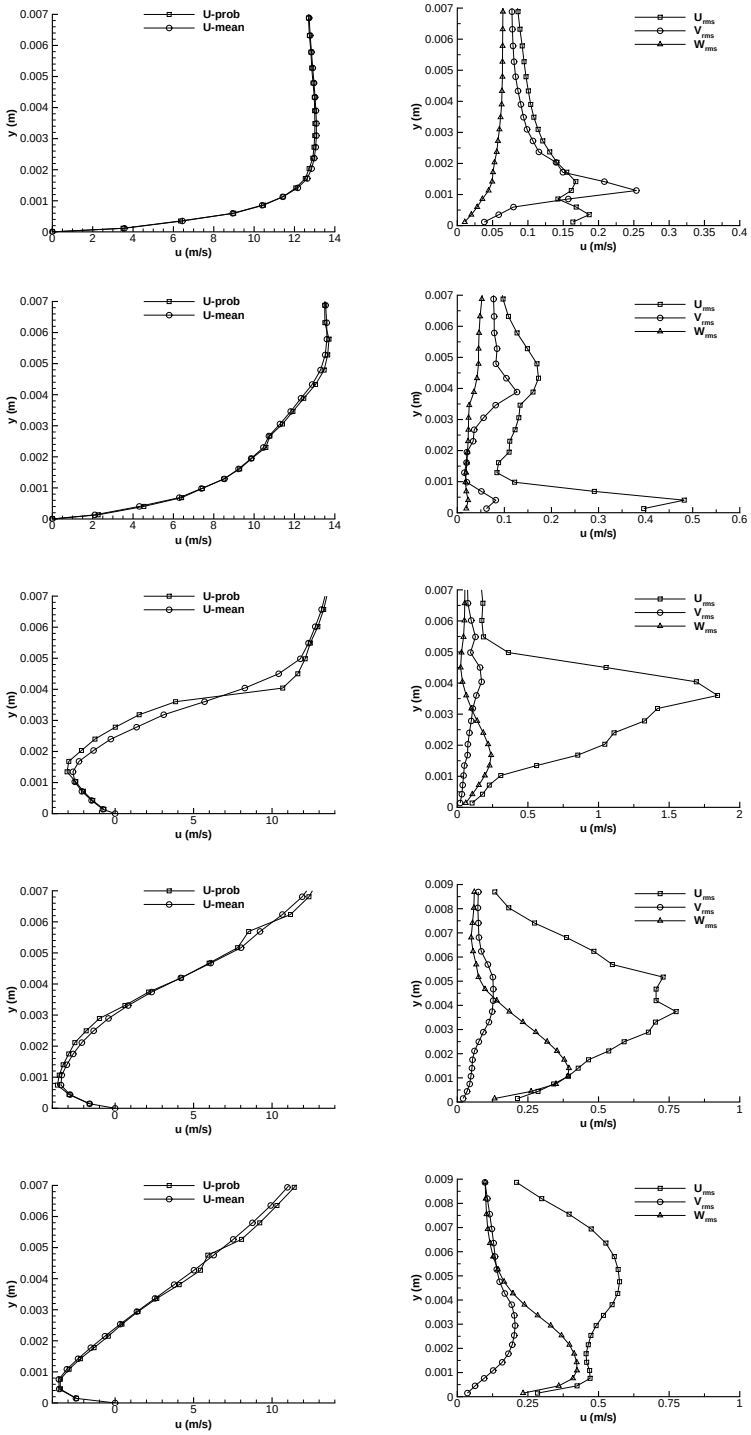

Figure 16: Time-averaged and most probable longitudinal velocity u (left) and RMS of the resolved part of the fluctuating velocities (right) in the mid-span from station 1 (top) to 5 (bottom).

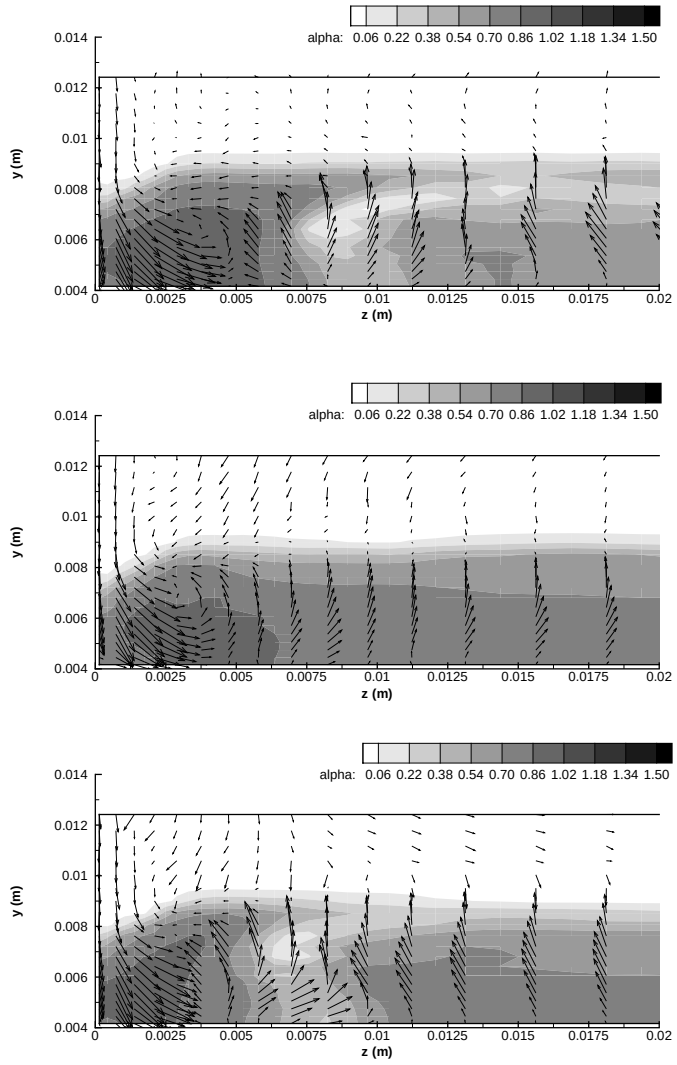

Figure 17: Snapshot of the void ratio and the velocity vector in a transversal cutting plane at station 3.

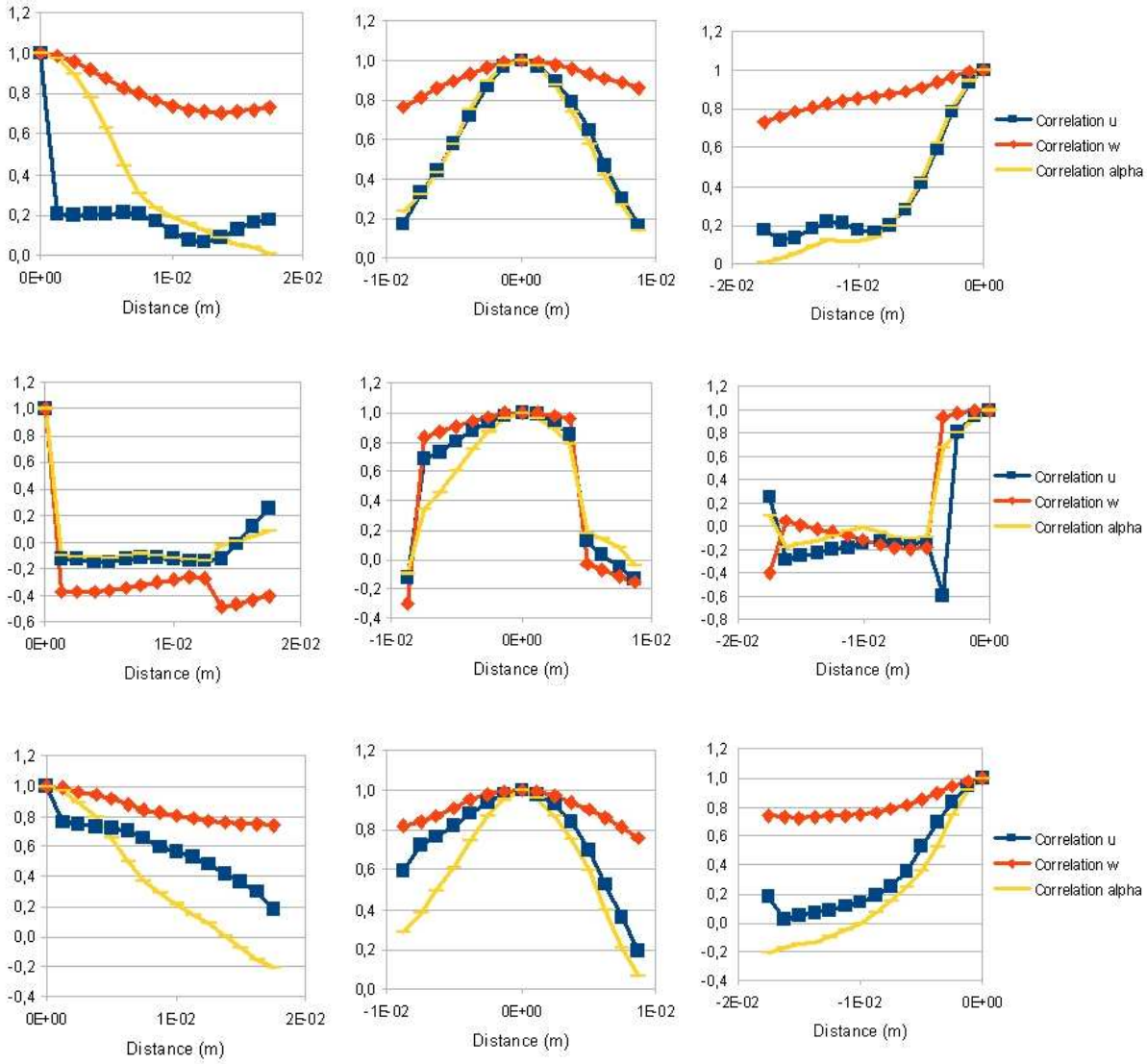

Figure 18: Spatial correlations based on the void fraction, the longitudinal and transversal velocities with three reference points: third-span (left), mid-span (middle) and two-third-span (right) and at three distances from the bottom wall: $y = 5$ mm, $y = 6.4$ mm and $y = 7.2$ mm (top to bottom).

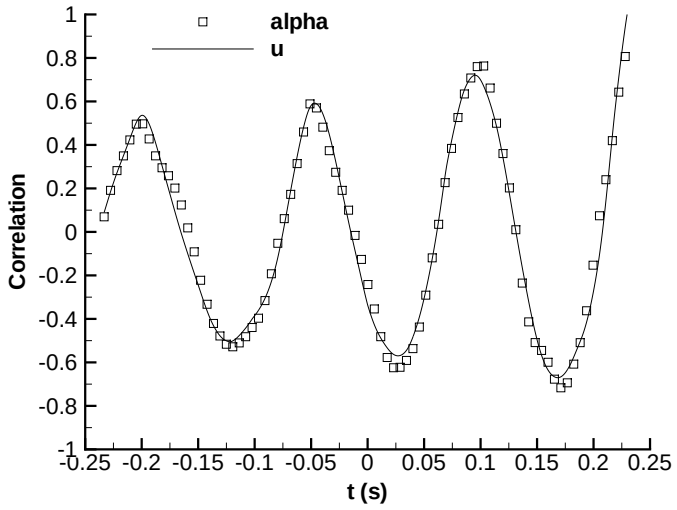

Figure 19: Spatial correlations based on the void fraction and the longitudinal velocity between two points located on each side of the Venturi.